Nano Research

ISSN 1998-0124 CN 11-5974/O4
https://doi.org/10.26599/NR.2026.94909020

Research Article

Zn^{2+}-doped Cs-Cu-I perovskite nanocrystals for white light-emitting diodes with high color rendering index

Jie Chen[1], Zhe Yin[1](✉), Tao Yin[2], Jinxing Zhao[2], Yu Li[1], Li Guan[2], Feng Teng[1](✉), Aiwei Tang[1](✉)

[1] Key Laboratory of Luminescence and Optical Information, Ministry of Education, School of Physical Sciences and Engineering, Beijing Jiaotong University, Beijing 100044, China

[2] Hebei Key Laboratory of Photo-Electricity Information and Materials, College of Physics Science and Technology, Hebei University, Baoding 071002, China

Nano Res., **Just Accepted Manuscript** • https://doi.org/10.26599/NR.2026.94909020

https://www.sciopen.com/journal/1998-0124 on Jul. 12, 2026

Just Accepted

Zn^{2+}-doped Cs-Cu-I perovskite nanocrystals for white light-emitting diodes with high color rendering index

Jie Chen [1], Zhe Yin [1 *], Tao Yin [2], Jinxing Zhao [2], Yu Li [1], Li Guan [2], Feng Teng [1 *], Aiwei Tang [1 *]

[1] Beijing Jiaotong University, China
[2] Hebei University, China

E-mail: awtang@bjtu.edu.cn
fteng@bjtu.edu.cn
zheyin@bjtu.edu.cn

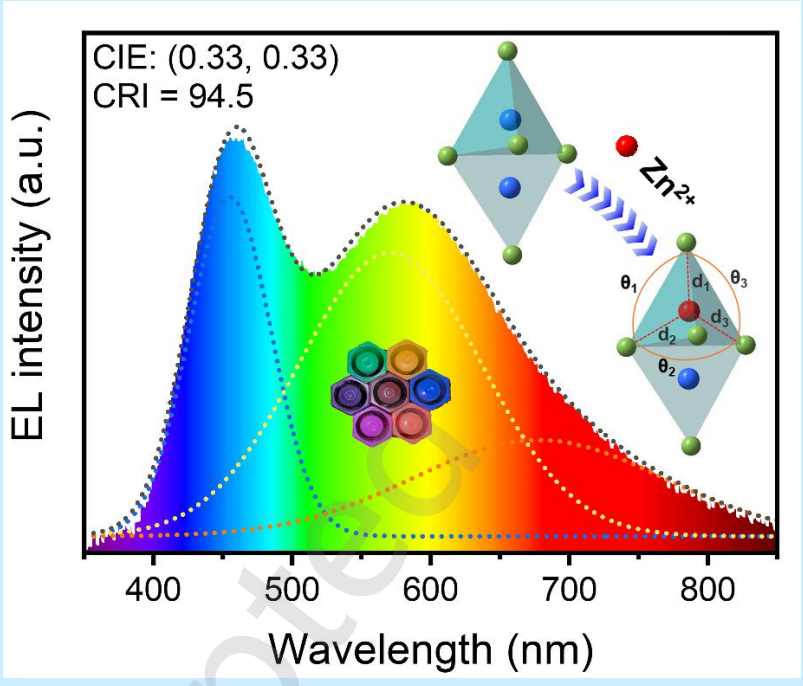

This work provides a Zn^{2+} doping strategy to boost the optical performance of $Cs_3Cu_2I_5$ nanocrystals via enhanced self-trapped exciton formation, subsequently enabling the fabrication of a white LED with standard white light and high color rendering index.

Nano Research

Open Access

Research Article

Zn^{2+}-doped Cs-Cu-I perovskite nanocrystals for white light-emitting diodes with high color rendering index

Jie Chen [1], Zhe Yin [1] ✉, Tao Yin [2], Jinxing Zhao [2], Yu Li [1], Li Guan [2], Feng Teng [1] ✉, and Aiwei Tang [1] ✉

[1] *Key Laboratory of Luminescence and Optical Information, Ministry of Education, School of Physical Sciences and Engineering, Beijing Jiaotong University, Beijing 100044, China*

[2] *Hebei Key Laboratory of Photo-Electricity Information and Materials, College of Physics Science and Technology, Hebei University, Baoding 071002, China*

Received: 30 May 2026; **Revised:** 4 July 2026; **Accepted:** 12 July 2026

✉ Address correspondence to Aiwei Tang, awtang@bjtu.edu.cn; Feng Teng, fteng@bjtu.edu.cn; Zhe Yin, zheyin@bjtu.edu.cn

Cite this article: *Nano Research*, 2026, 19, 94909020 https://doi.org/10.26599/NR.2026.94909020

ABSTRACT: Cs-Cu-I perovskites have shown great potential in white light-emitting diodes (WLEDs) due to their unique self-trapped exciton (STE) radiative recombination with broad emission. However, their relatively low photoluminescence quantum yield (PLQY) limits practical applications. Here, we significantly enhance the PLQY of $Cs_3Cu_2I_5$ nanocrystals from 56% to 86% simply via Zn^{2+} aliovalent doping. Density functional theory calculations and temperature-dependent photoluminescence spectra reveal that Zn^{2+} preferentially occupies the tetrahedral Cu site, introducing a shallow defect level as an efficient radiative recombination center. Meanwhile, the Zn^{2+} doping increases the exciton binding energy to 309.5 meV and reconstructs electron-phonon coupling, thereby promoting the formation of STE. Furthermore, a white-emitting Cs-Cu-I mixture consisting of blue-emitting $Cs_3Cu_2I_5$ and yellow-emitting $CsCu_2I_3$ is obtained in situ via a one-pot method by adjusting the reaction temperature without post- synthesis ratio adjustment. Based on this, a WLED with Commission Internationale de l'Éclairage (CIE) coordinates of (0.31, 0.33) and a color rendering index (CRI) of 89.2 is fabricated. Moreover, double perovskite ($Cs_2Na_{1-x}Ag_xIn_{1-y}Bi_yCl_6$, λ_{em} = 622 nm) is introduced to compensate for the insufficient red emission. The resulting WLED achieves standard white light with CIE coordinates of (0.33, 0.33), a high CRI of 94.5, and an R_9 value of 84. This device also exhibits excellent operational and environmental stability, along with an ultra-wide beam angle of 177°. This work not only clarifies the mechanism of ion doping in 0D perovskites but also provides a new pathway for constructing high-quality, environmentally friendly WLEDs for solid-state lighting.

KEYWORDS: $Cs_3Cu_2I_5$, nanocrystals, Zn^{2+} doping, white light-emitting diode

1 Introductions

With the rapid development of solid-state lighting technology, light-emitting diodes (LEDs) have surpassed traditional light sources as an efficient, energy-saving, and environmentally friendly lighting solution [1, 2]. In recent years, white LEDs (WLEDs) have received extensive attention, and their performance highly depends on the luminescence efficiency, spectral quality, and stability of emitting materials. Currently, commercial WLEDs mainly use blue LED chips to excite yellow phosphors (e.g., YAG: Ce^{3+}) to achieve white light output, but suffer from insufficient red components, poor spectral continuity, and low color rendering index (CRI), making it difficult to meet the requirements of high-quality lighting [3, 4]. Therefore, it is of great significance to develop new, efficient, environmentally friendly, and spectrally tunable luminescent materials. Pb-free halide perovskites have attracted attention due to their tunable structure and excellent optical properties. Among them, Cs-Cu-I, as a typical all-inorganic Cu-based halide perovskite, possesses a stable crystal structure and unique self-trapped exciton (STE) luminescence properties, exhibiting broad emission and a large Stokes shift, making it highly valuable for white lighting systems [5, 6]. However, its luminous efficiency is still low.

The emission of Cs-Cu-I is dominated by STE, and its luminescence efficiency is highly correlated with lattice distortion, defect state distribution, and phase structure stability [7-10]. Therefore, optimizing the lattice environment and defect state distribution is key to enhancing its luminescence performance. Ion doping is an effective strategy for tuning the optoelectronic properties of materials [11-14]. By introducing appropriate external ions, the local lattice environment and defect state distribution can be regulated without significantly damaging the host crystal structure [15, 16]. Compared with isovalent doping, aliovalent doping can adjust the local structure and suppress intrinsic defects through charge compensation, thereby reducing non-radiative recombination. In Cu-based halide perovskite systems, aliovalent doping shows greater advantages in defect engineering and stability regulation. Zn^{2+} has an ionic radius similar to that of Cu^{+}, and both have

$3d^{10}$ orbitals. Since the d^{10} orbital of Zn^{2+} has a stable closed-shell structure and does not introduce any additional Jahn-Teller active centers, doping with Zn^{2+} will not alter the inherent STE emission mechanism. Furthermore, the substitution of Cu^{+} by Zn^{2+} introduces charge compensation, which may alter the Cu-I coordination environment and lattice rigidity, thus affecting STE formation and exciton dynamics.

Improving luminescence efficiency and expanding the spectral range are key to achieving high-quality WLEDs. Previous studies have revealed a temperature-dependent phase transition between $Cs_3Cu_2I_5$ and $CsCu_2I_3$, and a blue-yellow mixture can be obtained by increasing the temperature, providing a new route for constructing white light systems [17, 18]. However, this mixture has slightly inadequate spectral coverage in the red region, resulting in a low CRI. Therefore, selecting efficient and stable red-emitting materials is crucial for achieving a high CRI. Currently, Sn-based perovskites suffer from poor stability, easy fluorescence quenching, and complex preparation [19-21]; organic-inorganic hybrid perovskites have poor environmental stability and are prone to thermal decomposition [22]; Mn^{2+} doping can introduce yellow emission but has limited spectral coverage [23-28]; rare-earth metal ion doping is costly and difficult to introduce [4, 29]. In contrast, the all-inorganic double perovskite $Cs2Na_{1-x}Ag_xIn_{1-y}Bi_yCl_6$ can be prepared by a simple low-temperature solution method, exhibiting excellent structural stability, thermal stability, and broad-band red emission with 622 nm. Importantly, it can be excited by 310 nm UV light, effectively compensating for the lack of red emission. Combined with the blue-yellow broad-spectrum emission of Cu-based perovskites, it is expected to form a continuous spectrum, achieving a high CRI and stable Commission Internationale de l'Éclairage (CIE) coordinates [30].

In this work, Zn^{2+}-doped $Cs_3Cu_2I_5$ nanocrystals (NCs) were successfully synthesized by a hot-injection method. The photoluminescence quantum yield (PLQY) was increased from 56% to 86%, while the stability and phase transition temperature were also improved. Temperature-dependent spectroscopy and density functional theory (DFT) calculations revealed the mechanism of the doping and performance enhancement. Furthermore, by taking advantage of the temperature-dependent phase transition, a mixture of blue-emitting $Cs_3Cu_2I_5$ and yellow-emitting $CsCu_2I_3$ was prepared. This film was integrated with a GaN chip (λ_{em} = 310 nm) to fabricate a WLED with CIE coordinates of (0.31, 0.33) and a CRI of 89.2. To optimize the color rendering performance, a double perovskite with an emission at 622 nm was introduced to supplement the red region, finally achieving a standard WLED with a CRI as high as 94.5 and CIE coordinates of (0.33, 0.33).

2 Results and discussion

Cs-Cu-I perovskite exhibits temperature-dependent phase transition behavior and shows potential for fabricating WLEDs. However, their PLQY is relatively low, which still falls far short of the requirements for practical WLED applications. Therefore, improving the PLQY is a key issue that needs to be urgently addressed. Ion doping is widely used as an effective material modification strategy. In this work, we synthesized Zn^{2+}-doped $Cs_3Cu_2I_5$ NCs by a hot-injection method. By adjusting the reaction temperature, we prepared a mixture consisting of blue-emitting $Cs_3Cu_2I_5$ and yellow-emitting $CsCu_2I_3$, which was then integrated with a GaN chip (λ_{em} = 310 nm) to fabricate a high-quality WLED. This study lays a solid theoretical and experimental foundation for advancing environmentally friendly perovskite luminescent materials toward practical applications in solid-state lighting. To minimize halogen vacancy defects, ZnI_2 was selected as the doping source to provide an iodine-rich environment. According to the different amounts of ZnI_2 added, the obtained samples were named as $Cs_3Cu_2I_5$: x% Zn (x = 0, 2.5, 5.0, 7.5, 10). Transmission electron microscopy (TEM) characterization and size distribution results are shown in Figure 1a, b and Figure S1. With increasing Zn^{2+} feeding amount, the morphology of the synthesized NCs remains unchanged, but their average size gradually decreases from 25.6 ± 1.8 to 20.1 ± 1.3 nm, and the size stabilizes when the doping ratio exceeds 5%. High-resolution TEM (HRTEM) images are shown in the inset of Figure 1a. Both undoped and doped samples display clear lattice fringes, indicating excellent crystallinity. Measurement results show that after Zn^{2+} doping, the lattice fringe spacing decreases from 3.53 to 3.43 Å, indicating lattice contraction induced by Zn2+ doping. X-ray diffraction (XRD) patterns show that all diffraction peaks of the samples are in excellent agreement with the standard card of pure-phase $Cs_3Cu_2I_5$ (PDF#79-0333), and no significant shift of diffraction peaks is observed before and after doping (Figure S2a, b).

To further quantify the doping concentration, inductively coupled plasma optical emission spectroscopy (ICP-OES) was used to accurately determine the actual Zn^{2+} content. As shown in Figure S2c, the actual Zn^{2+} doping amount increases nonlinearly with the feeding ratio. At low feeding ratios (2.5% and 5%), the actual doping amount is significantly lower than the feeding value, indicating that Zn^{2+} doping is relatively inefficient during the initial crystal formation stage and is subject to a certain degree of rejection. In contrast, at higher feeding ratios (7.5% and 10%), the actual Zn/Cu ratio is significantly higher than the feeding ratio, indicating that Zn^{2+} doping is not simply an isovalent substitution but may be accompanied by the adsorption of ZnI_2 on the surface. It can passivate Cu vacancy defects on the surface, which is conducive to improving the PLQY of NCs. Furthermore, the high-angle annular dark-field scanning TEM (HAADF-STEM) image and the corresponding energy-dispersive X-ray spectroscopy (EDS) elemental mapping of the $Cs_3Cu_2I_5$: 7.5% Zn sample clearly show that Cs, Cu, I, and Zn elements are uniformly distributed within the nanocrystals, confirming the successful doping of Zn^{2+} from a spatial distribution perspective (Figure 1c). To deeply investigate the chemical states of each element before and after doping, X-ray photoelectron spectroscopy (XPS) analysis was performed. As shown in Figure S3, the binding energies of Cs 3d and I 3d correspond to the +1 and -1 valence states, respectively, while the binding energy and spectral shape of Cu 2p clearly indicate the +1 valence state, and no characteristic satellite peaks of Cu^{2+} are detected.

This indicates that the oxidation of Cu^{+} is effectively suppressed during the entire synthesis process. Although a slight negative shift of about 0.2-0.3 eV is observed for the binding energies of Cs 3d and Cu 2p, this shift is within the instrument error range and thus cannot be used as a reliable indicator of changes in the chemical environment. Notably, in the spectrum of the Zn-doped sample, characteristic peaks at 1024.1 eV (Zn $2p_{3/2}$) and 1042.0 eV (Zn $2p_{1/2}$) can be clearly observed, which confirms that Zn exists in the +2 valence state and provides strong evidence that Zn^{2+} has been successfully incorporated into the material system. Furthermore, XPS measurement indicates that the Zn/Cu ratio is 5.6%, while ICP measurement shows that the ratio is 8.6%. This further indicates that the Zn^{2+} doping is not a simple substitutional doping. It may partially adsorb on the surface of the NCs (Figure 1d).

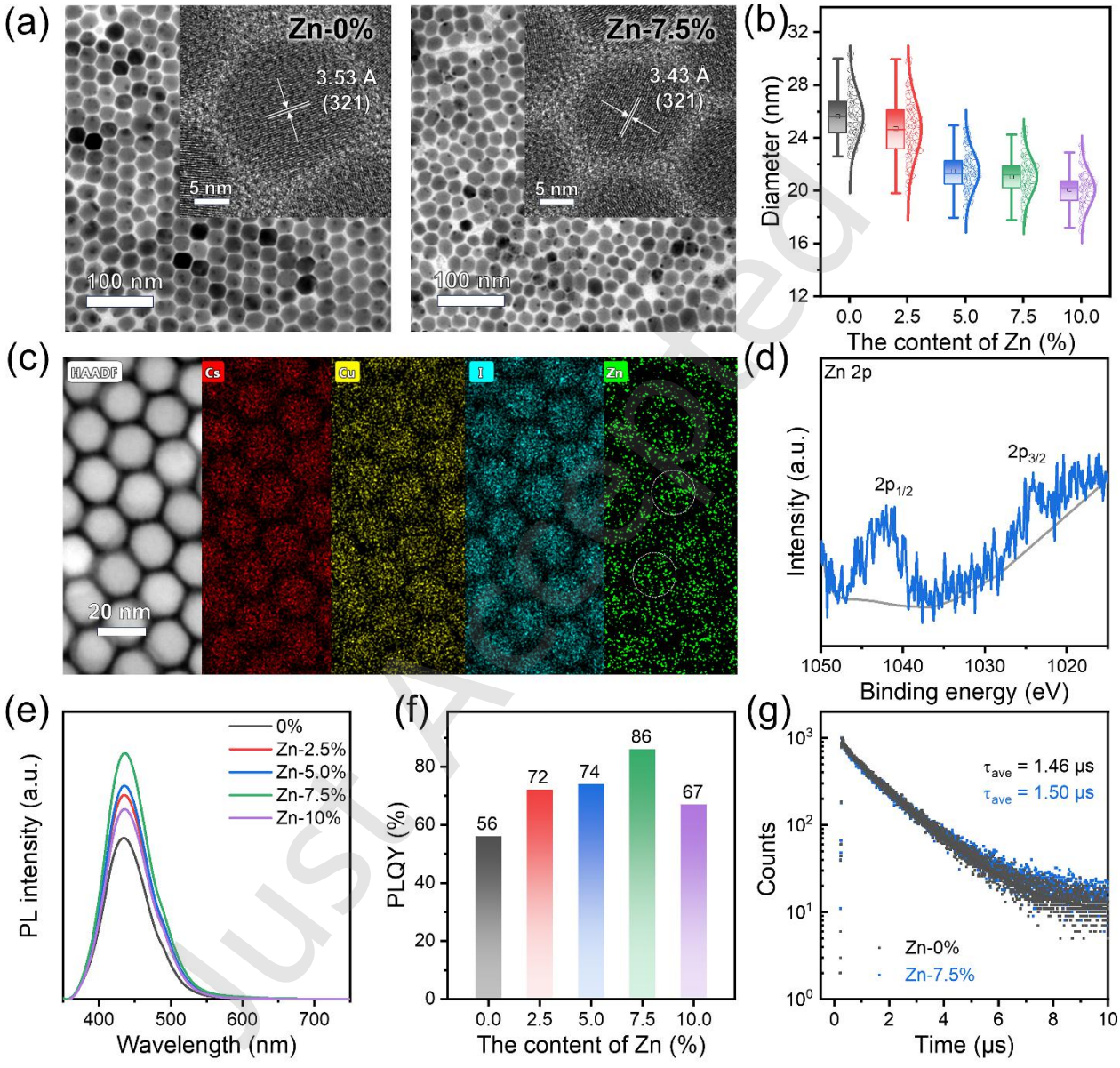

Figure 1. (a) TEM images of undoped $Cs_3Cu_2I_5$ and $Cs_3Cu_2I_5$: 7.5% Zn. (b) Size distribution of $Cs_3Cu_2I_5$: Zn. (c) HAADF-STEM images and the corresponding STEM-EDS elemental mapping images of $Cs_3Cu_2I_5$: 7.5% Zn. (d) XPS spectra of Zn ($2p_{1/2}$ and $2p_{3/2}$) in $Cs_3Cu_2I_5$: 7.5% Zn. (e) PL spectra and (f) the corresponding PLQY of $Cs_3Cu_2I_5$: Zn. (g) TRPL decay curves of undoped $Cs_3Cu_2I_5$ and $Cs_3Cu_2I_5$: 7.5% Zn.

Zn^{2+} doping has a positive effect on the luminescence properties of $Cs_3Cu_2I_5$ NCs. The photoluminescence (PL) spectra of $Cs_3Cu_2I_5$: Zn under 290 nm UV excitation are shown in Figure 1e. All samples exhibit a bright broadband blue emission peak at around 440 nm, indicating that the incorporation of Zn^{2+} does not change the STE emission mechanism. With increasing Zn^{2+} doping concentration, both the emission intensity and the PLQY first increase and then decrease, reaching the highest value of 86% at a feeding ratio of 7.5% (Figure 1f). To deeply investigate the effect of doping on exciton dynamics, time-resolved photoluminescence (TRPL) spectra of $Cs_3Cu_2I_5$ and $Cs_3Cu_2I_5$: 7.5% Zn were analyzed (Figure 1g). Fitting with a single-exponential function yields an average carrier lifetime of 1.46 μs for $Cs_3Cu_2I_5$, which slightly increases to 1.50 μs for $Cs_3Cu_2I_5$: 7.5% Zn. Both samples exhibit slow decay characteristics on the microsecond timescale, further confirming that the emission originates from STE recombination rather than fast

band-edge emission of a direct bandgap. Absorption spectra are shown in Figure S4. All samples exhibit a distinct absorption peak at around 290 nm, and a large Stokes shift of about 150 nm from the emission peak is observed. This effectively avoids self-absorption of the emitted light and is a typical feature of STE emission. The Tauc plots were obtained by converting the Kubelka-Munk function ($(\alpha h\nu)^2$-$h\nu$), as shown in the inset of Figure S4. The calculated optical bandgap of $Cs_3Cu_2I_5$ is 4.17 eV, while that of $Cs_3Cu_2I_5$: 7.5% Zn slightly decreases to 4.15 eV, which may be related to the lattice contraction and fine-tuning of the electronic structure induced by doping. However, such a subtle bandgap narrowing suggests that the doping-induced changes in luminescence performance are not primarily due to modulation of the bandgap but are more likely related to the reconstruction of electronic states within the bandgap. This finding provides an important basis for subsequent electronic structure analysis.

To further explain the intrinsic physical mechanism by which Zn^{2+} doping enhances the luminescence performance of $Cs_3Cu_2I_5$ NCs, DFT calculations were performed for in-depth analysis. The crystal structure of $Cs_3Cu_2I_5$ is shown in Figure 2a. In this lattice, there are two Cu sites with different coordination environments: Cu1 is tetrahedrally coordinated, while Cu2 is trigonally coordinated. First, the formation energy of Zn^{2+} occupying different sites was calculated, and the results are shown in Figure S5. Zn^{2+} has the lowest formation energy at the Cu1 site, indicating that it thermodynamically prefers to substitute the tetrahedrally coordinated Cu1. The bond lengths, bond angles, and lattice parameters between the B-site atom and the coordinated I atoms of $Cs_3Cu_2I_5$ and $Cs_3Cu_2I_5$: Zn were systematically calculated (Figure S6 and Table 1). The calculation results show that, compared with $Cs_3Cu_2I_5$ NCs, the overall unit cell volume of $Cs_3Cu_2I_5$: Zn NCs decreases significantly, indicating that Zn^{2+} doping induces lattice contraction, which is fully consistent with the XRD and HRTEM results mentioned above. Furthermore, after Zn^{2+} doping, the B-I bond length increases while the I-B-I bond angle decreases. According to the hard-soft acid-base (HSAB) theory, I^- is a soft base that is easily polarized, while Cu^+ is a soft acid with low charge and easy deformation, leading to the formation of relatively short Cu-I bonds with pronounced covalent character. In contrast, Zn^{2+} belongs to the borderline acid (slightly hard), and when combined with the soft base I^-, the ionicity significantly increases, resulting in a longer Zn-I bond length than the Cu-I bond length, and the lattice becomes softer. Meanwhile, the directionality of ionic bonds is weaker than that of covalent bonds, and after the bond length increases, due to the spatial constraints of adjacent polyhedra and Cs^+ in the lattice, the I-Zn-I bond angle is forced to decrease. These structural distortions soften the local lattice and strengthen the electron-phonon coupling, thereby facilitating STE formation and enhancing the luminescence performance. To further reveal the effect of Zn^{2+} doping on the electronic structure, the density of states (DOS) of the system was calculated, as shown in Figure S7. For intrinsic $Cs_3Cu_2I_5$, the valence band maximum and conduction band minimum are mainly contributed by Cu d and I p orbitals. After Zn^{2+} doping, an impurity energy level formed by the hybridization of I p and Zn s orbitals is introduced into the bandgap. This impurity level is a shallow defect level favorable for luminescence, which can serve as an effective exciton capture and radiative recombination center, significantly increasing the radiative recombination probability. This corresponds well with the increased PLQY (86%) and the slightly extended average carrier lifetime (1.50 μs) of the Zn^{2+}-doped samples. Therefore, Zn^{2+} doping does not simply modulate the lattice rigidity but rather introduces a new emission channel by reconstructing the emission center.

To further define the mechanism by which doping enhances the luminescence performance of $Cs_3Cu_2I_5$ NCs, the PL spectra of $Cs_3Cu_2I_5$ and $Cs_3Cu_2I_5$: 7.5% Zn were measured under variable-temperature conditions (Figure 2b, c). The results show that both samples exhibit typical thermal quenching behavior, with the emission intensity decreasing monotonically as the temperature rises. The integrated intensity of the PL spectra at different temperatures was fitted using the Arrhenius equation (Eq. (1)) to obtain the exciton binding energy (E_b):

$$I(T) = \frac{I_0}{1 + A\exp\left(-\frac{E_b}{k_B T}\right)} \quad (1)$$

Here, $I(T)$ is the integrated PL intensity at temperature T, I_0 is the initial integrated PL intensity, A is the pre-exponential factor, and k_B is the Boltzmann constant. The fitting results are shown in Figure 2d. The E_b of the $Cs_3Cu_2I_5$: 7.5% Zn reaches 309.5 meV, which is significantly higher than that of the undoped $Cs_3Cu_2I_5$ (104.7 meV). This indicates that Zn^{2+} doping substantially enhances the degree of exciton confinement, thereby effectively suppressing thermal dissociation of carriers and non-radiative recombination processes. This is one of the key physical reasons why Zn^{2+} doping significantly improves the PLQY. The notable increase in E_b means that excitons are more difficult to dissociate thermally at room temperature, thus suppressing the luminescence quenching process induced by thermal excitation. As a result, the doped sample maintains a relatively strong radiative recombination capability even under elevated temperature conditions, which is consistent with the experimental observation of a lower quenching degree in the doped sample during the temperature-dependent PL measurements.

Furthermore, the electron-phonon coupling strength was further investigated by analyzing the temperature dependence of the full width at half maximum (FWHM). The Huang-Rhys (S) factor and the average phonon energy ($\hbar\omega_{phonon}$) were obtained by fitting with Eq. (2):

$$FWHM = 2.36\sqrt{S}\ \ \omega_{phonon}\sqrt{\coth\frac{\omega_{phonon}}{2k_B T}} \quad (2)$$

The fitting results are shown in Figure 2e. For undoped $Cs_3Cu_2I_5$, the S factor is 34.6 and $\hbar\omega_{phonon}$ is 22.3 meV. After Zn^{2+} doping, the S factor significantly increases to 38.4, while $\hbar\omega_{phonon}$ decreases to 20.4 meV. This indicates that Zn^{2+} doping effectively modulates the electron-phonon coupling behavior.

Based on these results, the mechanism of the improved

luminescence performance can be revealed. Zn^{2+} directly substitutes Cu^{+} in the luminescent center $[Cu_2I_5]^{3-}$ dimer, inducing significant local lattice distortion (increased bond lengths and decreased bond angles). On one hand, this distortion enhances the overall coupling strength between excitons and lattice vibrations (increase in S). On the other hand, it introduces more low-frequency local soft mode vibrations, leading to a reduction in the average energy of the coupled phonons (decrease in $\hbar\omega_{phonon}$). In the STE emission system, this combination of strong coupling and low phonon energy facilitates efficient lattice relaxation of excitons through a multi-phonon process, promoting the formation of deep STE states [31]. Although an increase in S generally promotes multi-phonon non-radiative processes, the excitons are already strongly localized under this condition, making it difficult for them to migrate to defects, and thus, non-radiative recombination decreases instead. More importantly, DOS calculations show that Zn^{2+} doping introduces a shallow defect level in the bandgap, providing an efficient radiative recombination channel for excitons. Therefore, the enhanced electron-phonon coupling promotes exciton self-trapping and localization, while the shallow level ensures efficient radiative recombination. The synergistic effect of these two factors together leads to a significant increase in PLQY.

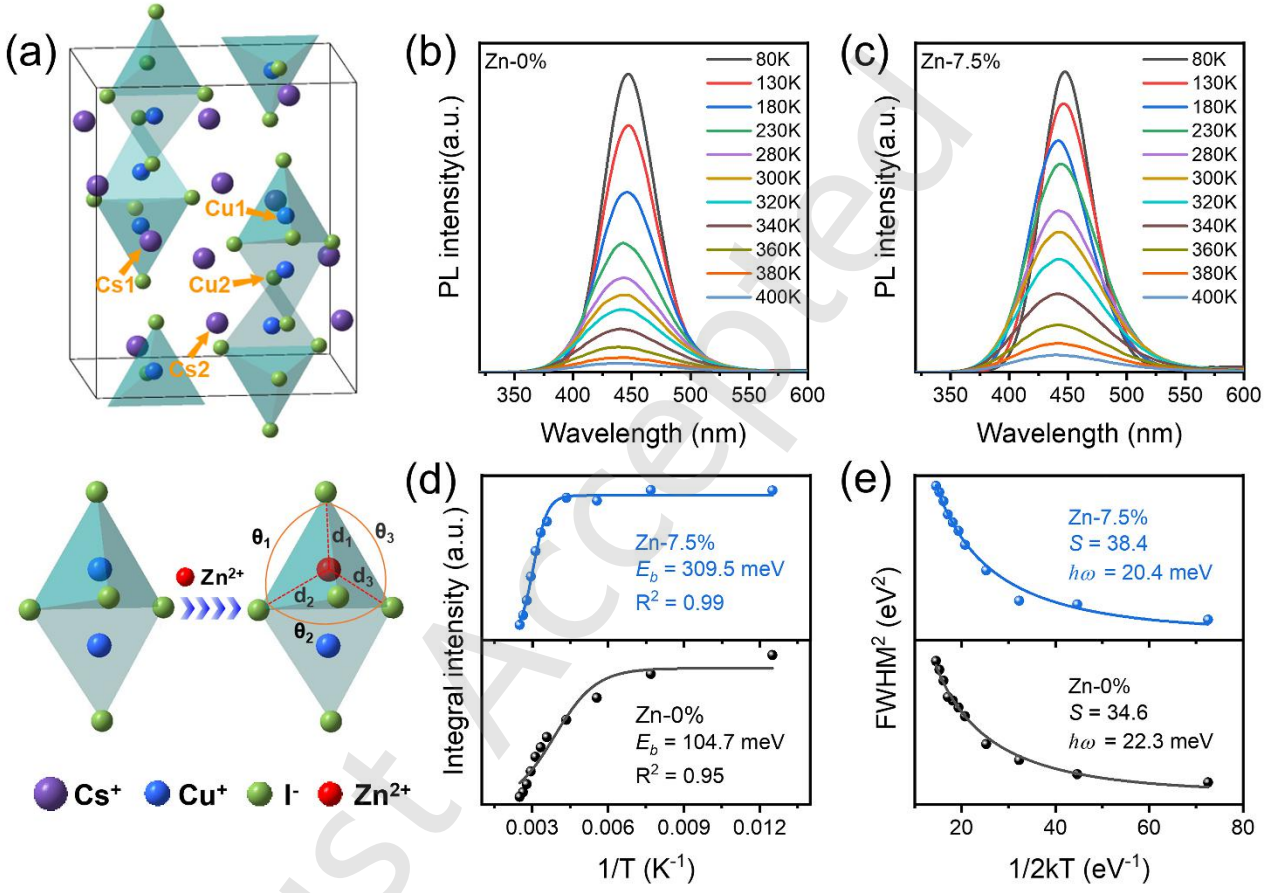

Figure 2. (a) Schematic diagrams of the crystal structure of $Cs_3Cu_2I_5$: Zn. (b, c) Temperature-dependent PL spectra, (d) the fitting curves between the PL integral intensity and the reciprocal temperature; and (e) the fitting curve between the square of FWHM and 1/2kT of $Cs_3Cu_2I_5$ and $Cs_3Cu_2I_5$: 7.5% Zn.

Under the optimal doping ratio (Zn-7.5%), the coexistence of blue-emitting $Cs_3Cu_2I_5$ and yellow-emitting $CsCu_2I_3$ was successfully synthesized in a single reaction system by adjusting the reaction temperature. XRD patterns show that the diffraction peaks of $CsCu_2I_3$ already appear at 130 °C in the undoped system, while the phase transition temperature of the doped system is significantly increased to 150 °C, indicating that Zn^{2+} doping enhances the stability of the $Cs_3Cu_2I_5$ phase (Figure S8). This is because after doping with Zn^{2+}, the smaller Zn^{2+} partially replaced the Cu^{+} sites, resulting in a slight contraction of the lattice and a denser and more stable crystal structure. Secondly, this behavior is related to the difference in structural dimensionality. The 0D structure of $Cs_3Cu_2I_5$ possesses isolated luminescent centers and a high exciton binding energy, making the modulation of the local electronic structure by doping more direct and effective. In contrast, in the 1D chain-like structure of $CsCu_2I_3$, the doping effect is distributed and transferred along the chains, leading to a relatively weaker regulation of structural stability [6, 31-34]. The one-step hot-injection synthesis of the two-phase coexistence system provides an ideal platform for white light emission in a single-material system.

To achieve uniform and stable luminescent films, various polymer matrices were used for preparation. It was found that PDMS is difficult to mix uniformly, epoxy resin causes luminescence quenching, and nanocrystals tend to precipitate out of polystyrene. In contrast, PMMA is soluble in toluene and shows good miscibility with the nanocrystals, resulting in a film with uniform dispersion and excellent luminescence properties after curing. Therefore, PMMA was

selected to prepare the Cs-Cu-I/PMMA film. PL spectra of films are shown in Figure S9. The ratio of the two phases can be controlled by adjusting the reaction temperature, thereby tuning the relative intensities of blue and yellow emission. The optimal excitation wavelengths of $Cs_3Cu_2I_5$ and $CsCu_2I_3$ are 290 nm and 325 nm, respectively. Therefore, one phase can also be preferentially excited by selecting the appropriate excitation wavelength in the same film. This synergistic modulation strategy based on phase composition and excitation wavelength selectivity enables continuously tunable color output without the need for mixing multiple luminescent components.

Since the GaN chip (λ_{em} = 310 nm) can effectively excite both the $Cs_3Cu_2I_5$ and $CsCu_2I_3$ phases simultaneously, generating blue and yellow light emissions, integrating the Cs-Cu-I/PMMA composite film with the GaN chip (λ_{em} = 310 nm) is used to fabricate LEDs. As shown in Figure 3a, Figure S10, and Table 2, the electroluminescence (EL) spectrum of the WLED fabricated with Cs-Cu-I: 7.5% Zn synthesized at 155 °C can be deconvoluted into a blue emission peak from $Cs_3Cu_2I_5$ and a yellow emission peak from $CsCu_2I_3$. The corresponding CIE coordinates are (0.31, 0.33), close to standard white light, and the CRI is improved to 89, which is significantly better than the device fabricated with Cs-Cu-I synthesized at 130 °C and meets the basic requirements for general solid-state lighting. However, the emission intensity of this device in the long-wavelength red region, especially near 700 nm, is still insufficient, resulting in a saturated red rendering index (R_9) value of only 34 (Figure 3b).

To obtain WLED with more comprehensive color rendering performance and higher light quality, the red-emitting double perovskite $Cs_2Na_{1-x}Ag_xIn_{1-y}Bi_yCl_6$ was introduced into the existing blue- yellow composite spectrum. The double perovskite material was synthesized by a low-temperature solution method. Scanning electron microscopy (SEM) and EDS mapping showed that Cs, Na, Ag, In, Bi, and Cl elements are uniformly distributed in the double perovskite particles (Figure S11a). EDX spectrum revealed that the atomic ratio of Cs: Na: Ag: In: Bi: Cl was consistent with the expected composition (Figure S11b and Table 3). The XRD pattern shows that the diffraction peaks of the obtained product agree well with the standard cards of $Cs_2NaInCl_6$ and $Cs_2AgInCl_6$ reported, indicating a face-centered cubic double perovskite structure (Figure S11c) [35]. XPS spectra show characteristic peaks of Cs, Na, Ag, In, Bi, and Cl elements, consistent with their expected oxidation states (Cs^+, Na^+, Ag^+, In^{3+}, Bi^{3+}, and Cl^-) in the double perovskite, confirming successful synthesis (Figure S12).

The optical properties of the double perovskite powder and film were characterized. As shown in Figure S13a, both exhibit a broad emission peak around 622 nm, effectively complementing the red region from 600 to 800 nm. Compared with powder, film shows a slight redshift together with a marginally broader FWHM, which is likely attributed to the altered local dielectric environment and subtle interparticle interactions after embedding powders into PDMS. Meanwhile, there are two excitation peaks at 300 nm and 360 nm, indicating that the double perovskite can be efficiently excited by UV light around 300 nm, and the emission peak position does not change with the excitation wavelength (Figure S13b-d). The absolute PLQY under 310 nm excitation is 40.7% (Figure S13e). The time-resolved PL (TRPL) decay curve was fitted with a double-exponential function, yielding an average carrier lifetime of 14.0 μs (Figure S13f and Table 4). This slow decay on the microsecond timescale is consistent with the STE recombination mechanism, indicating that the emission does not originate from fast band-edge transitions of a direct bandgap.

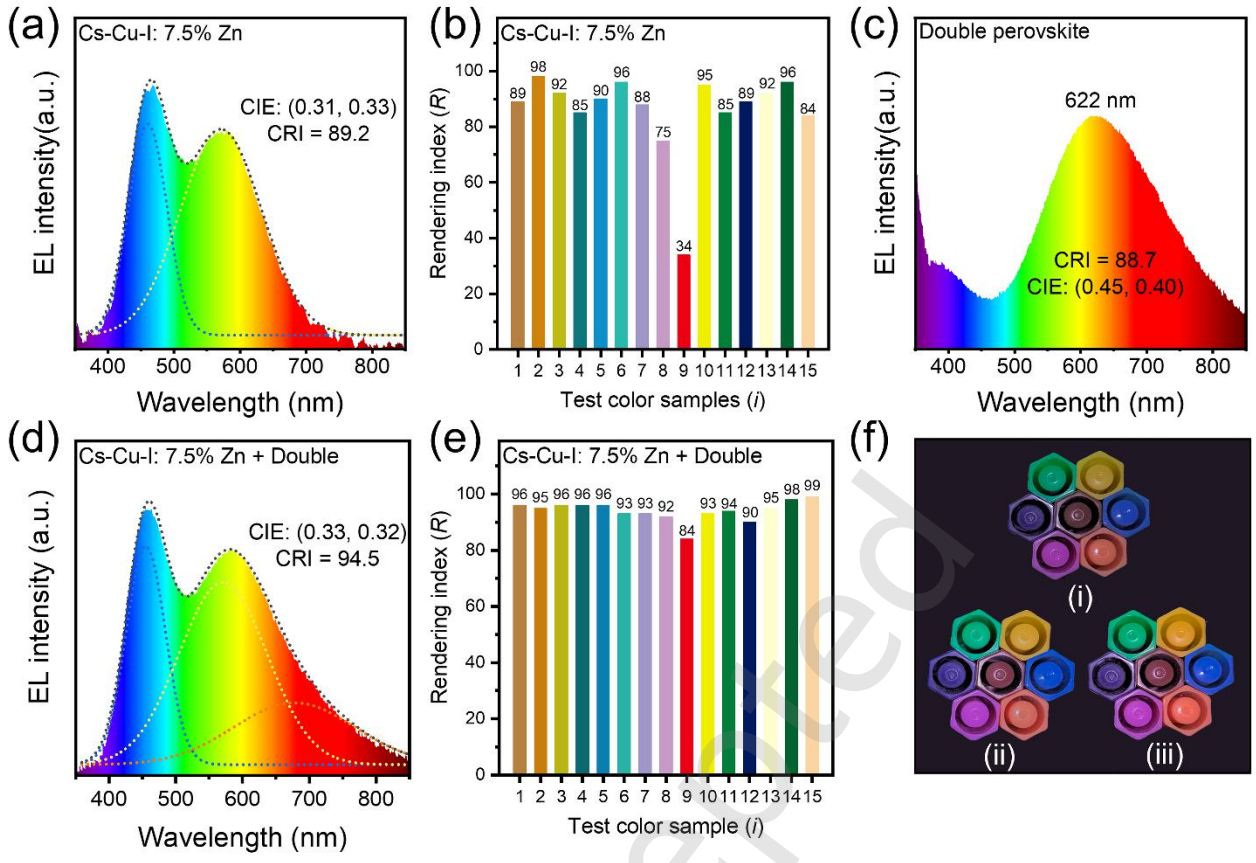

Figure 3. (a) EL spectrum and (b) R_1-R_{15} special color rendering index of the WLED device fabricated with Cs-Cu-I: 7.5% Zn. (c) EL spectrum of the LED device fabricated with double perovskite. (d) EL spectrum and (e) R_1-R_{15} special color rendering index of the WLED device fabricated based on Cs-Cu-I: 7.5% Zn and double perovskite. (f) Photographs of marker pens illuminated by WLEDs devices based on (i) Cs-Cu-I, (ii) Cs-Cu-I: 7.5% Zn, and (iii) Cs-Cu-I: 7.5% Zn + double perovskite, demonstrating their performance as lighting sources.

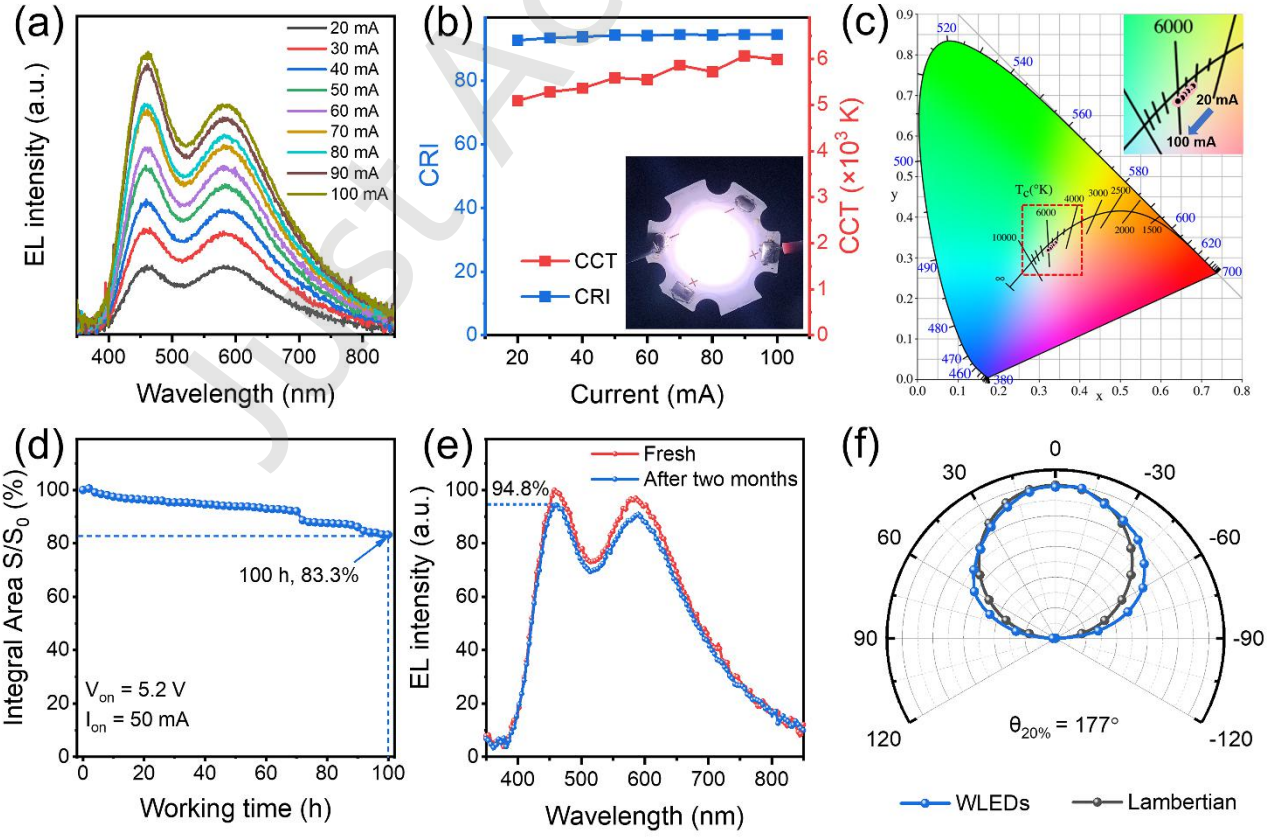

Figure 4. Stability characterization of the WLED fabricated based on Cs-Cu-I: 7.5% Zn + double perovskite under different driving currents: (a) EL spectra, (b) CRI and CCT, and (c) CIE 1931 chromaticity diagram. (d) Change in EL intensity before and after continuous operation for 100 hours at 5.2 V and 50 mA; (e) Change in EL spectra before and after storage in ambient laboratory conditions without temperature and humidity control for two

months. (f) spatial distribution of the beam radiation intensity of the device at the driving current of 20 mA.

The LED was fabricated by integrating the double perovskite film with a GaN chip emitting at 310 nm. Its EL spectrum (Figure 3c) shows a main peak at 622 nm, with CIE coordinates of (0.45, 0.40) and a CRI of 88.7. It effectively complements the red component, achieving an R_9 value of 54 (Figure S14). Furthermore, the double perovskite was combined with the Cs-Cu-I: 7.5% Zn blue- yellow composite system in an optimized ratio to fabricate a WLED (Figure 3d, e). Its EL spectrum under 70 mA can be deconvoluted into three characteristic peaks, corresponding to the blue emission of $Cs_3Cu_2I_5$, the yellow emission of $CsCu_2I_3$, and the red emission of the double perovskite. The CIE coordinates are stable at (0.33, 0.32), the CRI is further improved to 94.5, and the R_9 value increases to 84. This performance is among the best in similar systems (Table S6). When the driving current is 50 mA, the device exhibits CIE coordinates of (0.33, 0.33), exactly coinciding with the standard white point, with a CRI as high as 94.3 and an R_9 of 77 (Figure S15). The significant improvement in CRI is mainly attributed to the effective supplementation of the red spectral region by the double perovskite.

To evaluate the practical application effect of WLEDs fabricated with Cs-Cu-I, Cs-Cu-I: 7.5% Zn, and Cs-Cu-I: 7.5% Zn + double perovskite as light sources, the marker pens were photographed under illumination of each device (Figure 3f). In comparison, the photograph taken under the WLED based on Cs-Cu-I: 7.5% Zn + double perovskite shows more vivid colors, with color reproduction closer to the real objects, especially for orange- yellow and orange- red hues. The photograph taken under the WLED based on undoped Cs-Cu-I appears generally darker, mainly due to the low PLQY of Cs-Cu-I, resulting in insufficient device brightness. In contrast, the photograph taken under the WLED based on Cs-Cu-I: 7.5% Zn appears washed out with less distinct color gradations. These results indicate that the effective compensation of the red spectral region by introducing the double perovskite significantly improves the R_9 value, thereby playing an important role in enhancing the color rendering capability of the device.

To further evaluate the device performance, its optoelectronic characteristics under different driving currents were measured (Figure 4a-c and Table 5). As the current increases, the EL spectral intensity increases accordingly, while the emission peak position and spectral shape remain essentially unchanged. The CRI, correlated color temperature (CCT), and CIE coordinates only show slight variations. CIE always remains within the white light region, indicating stable optical performance over the investigated current range of the device. The fidelity index (R_f) of the device is always above 90, suggesting that it can achieve highly realistic color reproduction in solid-state lighting applications. The gamut index (R_g) ranges from 98.9 to 100.7, indicating that the device also possesses high color saturation, making object colors appear vivid and vibrant under illumination. In addition, the operational stability and environmental stability of the WLED were tested. After continuous operation at 5.2 V and 50 mA for 100 hours, the luminescence intensity remained at 83.3% of its initial value (Figure 4d), demonstrating good operational stability. Furthermore, after storing the device in a room-temperature environment for two months, the luminescence intensity retention rate was as high as 94.8% (Figure 4e), indicating excellent long-term stability of this WLED under conventional environmental conditions. Finally, the spatial distribution of the beam radiation intensity of the device was measured (Figure 4f). The angle corresponding to a drop in intensity to 20% of its maximum value ($\theta_{20\%}$) was 177°, which belongs to an ultra-wide beam angle. This indicates that the light spreads rapidly and uniformly over a large area after emission, facilitating glare-free, soft, and uniform large-area illumination.

3 Conclusions

In summary, the PLQY of $Cs_3Cu_2I_5$ NCs was significantly increased from 56% to 86% through a simple Zn^{2+} aliovalent doping strategy. Combined with temperature-dependent spectroscopy and DFT calculations, the mechanism was revealed: Zn^{2+} occupies the tetrahedral Cu site, introducing a shallow defect level as an efficient radiative recombination center, greatly increasing the exciton binding energy, while simultaneously reconstructing the electron-phonon coupling to promote STE formation. Meanwhile, a mixture of Zn^{2+}-doped blue-emitting $Cs_3Cu_2I_5$ and yellow-emitting $CsCu_2I_3$ was designed by adjusting the reaction temperature, which emits white light without any post- synthesis ratio adjustment. Furthermore, a double perovskite with broad emission was further introduced to fabricate the WLED with a standard CIE coordinates of (0.33, 0.33), a CRI as high as 94.5, and a saturated red index R_9 of 84, which is an important parameter for illumination. The device exhibits excellent stability and an ultra-wide beam angle of 177°. This work not only deeply studies the mechanism of ion doping on the luminescence properties of 0D perovskites but also paves a new way for achieving high-quality WLED based on Pb-free perovskites. It lays a solid theoretical and experimental foundation for advancing environmentally friendly perovskite toward practical applications in solid-state lighting.

4 Experimental

4.1 Materials

Cesium carbonate (Cs_2CO_3, 99.9%), cuprous iodide (CuI, 99.9%), zinc iodide (ZnI_2, 99.99%), cesium chloride (CsCl, 99.99%), sodium chloride (NaCl, 99.5%), oleic acid (OA, 90%), oleylamine (OM, 90%), and methylbenzene (99.5%) were purchased from Shanghai Aladdin Reagent Company. Indium chloride ($InCl_3$, 99.99%), polymethyl methacrylate (PMMA), and 1-octadecene (ODE, 90%) were purchased from Alfa Esha Chemical Co. LTD. Zinc acetate ($Zn(OAc)_2$, 99.99%) was procured from Shanghai Titan Technology Co., LTD. Silver chloride (AgCl, 99.5%) was procured from Beijing Inokai Technology Co., LTD. Bismuth chloride ($BiCl_3$,98%) was purchased from Sigma Aldrich (Shanghai) Trading Co., LTD. Polydimethylsiloxane (PDMS) was procured from Dow Corning (China) Investment Co., LTD. Concentrated hydrochloric acid (HCl, 36%~38%) was procured from Sinopharm Group Chemical Reagent Co., LTD. Ethyl alcohol was procured from Beijing Tongguang Fine Chemicals. N-

hexane was procured from Tianjin Fuyu Fine Chemical Co. LTD. All chemicals and materials were used as received without further purification.

4.2 Preparation of Cs-oleate precursor solution

0.814 g Cs_2CO_3, 2.5 mL OA and 40 mL ODE were loaded into a three-neck round-bottom flask. The reaction mixture was heated to 120 °C under vacuum and maintained at this temperature for 30 min to eliminate water and oxygen from the system. It is then heated in nitrogen until all Cs_2CO_3 was dissolved to obtain 0.1 mmol/mL Cs-oleate solution, which was stored in a sealed container. Since Cs-oleate solution tends to solidify at room temperature, it was preheated to 120 °C before hot injection for the synthesis below.

4.3 Synthesis of Cs-Cu-I: Zn NCs

0.4 mmol of CuI, x mmol of ZnI_2 (x = 0.01, 0.02, 0.03, 0.04), and 10 mL of ODE were placed in a 25 mL three-neck flask. The mixture was heated to 120 °C under vacuum with vigorous stirring for 30 min to remove residual water and dissolved oxygen, and to ensure thorough dispersion of the precursors. Then, while maintaining the temperature at 120 °C, 1 mL of OA and 1 mL of OM preheated to 70 °C were quickly injected. The reaction was allowed to proceed for another 5 min until the powder was completely dissolved. The atmosphere was then switched to nitrogen, and the reaction temperature was adjusted to T °C (T = 70, 90, 110, 130, 140, 150, 160, or 170). Subsequently, 4.0 mL of Cs- oleate precursor solution preheated to 125 °C was rapidly injected. The reaction was continued for 10 s, and then immediately stopped by placing the flask in an ice- water bath for 10 min. After cooling, the mixture was warmed with a blow dryer to melt the solids, transferred to a centrifuge tube, and centrifuged at 8000 rpm for 10 min. The supernatant was discarded, and the precipitate was collected for subsequent WLED device fabrication.

4.4 Preparation of $Cs_2Na_{1-x}Ag_xIn_{1-y}Bi_yCl_6$ double perovskite

2 mmol of CsCl, 0.9 mmol of NaCl, 0.1 mmol of AgCl, 0.95 mmol of $InCl_3$, and 0.05 mmol of $BiCl_3$ were placed in a 50 mL centrifuge tube. Then, 2.0 mL of concentrated hydrochloric acid was added, and the mixture was vigorously shaken for 10 min. The mixture was centrifuged at 5000 rpm for 10 min, and the supernatant was discarded. The precipitate was collected, washed twice with ethanol, and dried in a vacuum oven at 60 °C for 2 h. The obtained powder was ground and sieved before being used for WLED device fabrication [36].

4.5 Preparation of fluorescent films

PMMA was dissolved in toluene to prepare a 20 wt% solution. This solution was mixed with the $Cs_3Cu_2I_5$ NCs powder obtained from the first centrifugation and stirred vigorously for 24 h. The mixture was then dropped onto a glass slide and left in the air for 24 h to allow the solvent to evaporate completely, yielding a $Cs_3Cu_2I_5$ PMMA phosphor film. The A and B components of PDMS were mixed at a ratio of 10:1 and stirred evenly. Then, 0.3 g of the PDMS mixture was combined with 0.07 g of the sieved double perovskite powder and stirred. After removing air bubbles, the mixture was dropped onto a glass slide and left in the air for 24 h to form a double perovskite film.

4.6 Fabrication of WLED device

The as-prepared Cs-Cu-I film and double perovskite film were integrated with a GaN chip emitting at 310 nm to construct WLED devices for subsequent performance testing.

4.7 Characterization

The morphology and size of the samples were characterized by JEM-1400 (100 kV) transmission electron microscopy (TEM). Lattice fringes were measured by JEM-F200 (200 kV) high-resolution transmission electron microscopy (HRTEM). The X-ray diffraction (XRD) patterns were obtained by a Bruker D8 advance diffractometer using a Cu Kα radiation source (λ = 1.54056 Å). The element contents of the samples were measured by inductively coupled plasma-optical emission spectroscopy (ICP-OES) using American Agilent ICPOES730. X-ray photoelectron spectroscopy (XPS) measurements were carried out on a Thermo SCIENTIFIC ESCALAB 250Xi spectrometer with monochromatic Al Ka radiation using an anode voltage of 14.6 KV. All XPS peaks have been calibrated with the C1s peak (the binding energy of 284.80 eV). The absorption and transmission spectra were recorded using a UV-3600iplus spectrometer from transmission. The scanning electron microscope (SEM) images were captured using the Regulus 8100 cold field emission scanning electron microscope (FESEM). The elemental distribution map of the sample and the qualitative and semi-quantitative elemental composition spectra were obtained through the Bruker XFlash 6-30 (5 kV) X-ray energy dispersive spectroscopy instrument (EDS). PL spectra and photoluminescence excitation (PLE) spectra were obtained with a FLUORAT-02-PANORAMA spectrofluorometer. Temperature-dependent PL spectra were measured by Edinburgh FLS1000 and OptistatDN of Oxford Instruments plc, and the holding time for each temperature is 5 minutes. The time-resolution photoluminescence (TRPL) spectra measurements and absolute photoluminescence quantum yield were recorded by Edinburgh FLS1000 phosphorescence lifetime system and excited at wavelengths of 310 nm. The relative PLQY was measured by using rhodamine B as a standard reference (QY = 97%, in ethanol), calculated as Eq. (3):

$$QY_S = QY_R \times \frac{I_S}{I_R} \times \frac{A_R}{A_S} \times \frac{n_S^2}{n_R^2} \quad (3)$$

Where QY is the quantum yield, I is the measured integrated area of PL intensity, n is the refractive index (n = 1.375 for hexane; n = 1.362 for ethanol), and A is the absorbance at the excitation wavelength, which is typically lower than 0.10. The subscript R means Rhodamine B, and S means the as-obtained sample, all the data were measured under the excitation wavelength of 290 nm. All measurements were performed at room temperature. Electroluminescence (EL) Spectra, Commission Internationale de l'Éclairage (CIE), color rendering index (CRI), color fidelity index (R_f), color gamut index (R_g), and correlated color temperature (CCT) were measured using the Everfine HAAS-2000 high-precision and rapid spectral radiometer and the remote precise digital display DC regulated power supply. Beam angle (θ) was measured using

an Everfine LED distribution photometer.

Electronic Supplementary Material: Supplementary material (TEM images, XRD patterns, XPS spectra, absorption spectra, DFT calculations, PL spectra, EL spectra, FESEM image, EDS element mapping, EDX spectrum, TRPL decay curves) is available in the online version of this article at https://doi.org/10.26599/NR.2026.94909020.

Data availability

All data needed to support the conclusions in the paper are presented in the manuscript and the Electronic Supplementary Material. Additional data related to this paper may be requested from the corresponding author upon request.

Acknowledgements

This work is granted by the National Natural Science Foundation of China (No. 12274021, 12574429) and Beijing Natural Science Foundation (Z220007).

Declaration of competing interest

All the contributing authors report no conflict of interests in this work.

Author contribution statement

Jie Chen: Data curation, experimental design, validation, writing manuscript. Yu Li, and Jinxing Zhao: Experimental design, writing manuscript. Tao Yin, and Guan Li: Experimental design. Zhe Yin, Aiwei Tang, and Feng Teng: Project administration, funding acquisition, experimental design. All the authors have approved the final manuscript.

Use of AI statement

None.

References

[1] Zhao, S.; Mo, Q.; Wang, B.; Cai, W.; Li, R.; Zang, Z. Inorganic halide perovskites for lighting and visible light communication. *Photonics Res.* **2022**, *10*, 1039-1062.

[2] Luo, J.; Hu, M.; Niu, G.; Tang, J. Lead-free halide perovskites and perovskite variants as phosphors toward light-emitting applications. *ACS Appl. Mater. Interfaces* **2019**, *11*, 31575-31584.

[3] Islam, N. U.; Usman, M.; Rasheed, S.; Jamil, T. Review-white light-emitting diodes: past, present, and future. *ECS J. Solid State Sci. Technol.* **2021**, *10*, 106004.

[4] Oh, J. H.; Eo, Y. J.; Yoon, H. C.; Huh, Y.-D.; Do, Y. R. Evaluation of new color metrics: Guidelines for developing narrow-band red phosphors for WLEDs. *J. Mater. Chem. C* **2016**, *4*, 8326-8348.

[5] Zhang, X.; Zhou, B.; Chen, X.; Yu, W. W. Reversible transformation between $Cs_3Cu_2I_5$ and $CsCu_2I_3$ perovskite derivatives and its anticounterfeiting application. *Inorg. Chem.* **2021**, *61*, 399-405.

[6] Smith, M. D.; Karunadasa, H. I. White-light emission from layered halide perovskites. *Acc. Chem. Res.* **2018**, *51*, 619-627.

[7] Zeng, F.; Guo, Y.; Hu, W.; Tan, Y.; Zhang, X.; Yang, J.; Lin, Q.; Peng, Y.; Tang, X.; Liu, Z.; Yao, Z.; Du, J. Green anti-solvent assisted crystallization strategy for air-stable uniform $Cs_3Cu_2I_5$ perovskite films with highly efficient blue photoluminescence. *J. Lumin.* **2020**, *223*, 117178.

[8] Liu, C.; Zhang, Y.; Wang, L.; Chang, J.; Li, Q.; Zhang, X.; Bae, B. S.; Fayemi, O. E.; Xu, X.; Pan, J.; Chen, J.; Lei, W. Polymer-assisted crystal growth regulation and defect passivation for high-performance flexible solar-blind photodetectors based on copper-based halides. *J. Mater. Chem. C* **2024**, *12*, 1965-1971.

[9] Gao, F.; Zhu, X.; Feng, Q.; Zhong, W.; Liu, W.; Xu, H.; Liu, Y. Deep-blue emissive $Cs_3Cu_2I_5$ perovskites nanocrystals with 96.6% quantum yield via InI_3-assisted synthesis for light-emitting device and fluorescent ink applications. *Nano Energy* **2022**, *98*, 107270.

[10] Fan, W.; Zhang, K.; Wang, S.; Xu, L.; Liu, Y.; Song, J. A ligand strategy retarding monovalent copper oxidation toward achieving $Cs_3Cu_2I_5$ perovskite emitters with enhanced stability for lighting. *Nanoscale* **2023**, *15*, 16561-16570.

[11] Xiang, P.; Wei, Q.; Wang, C.; Cai, P.; Tong, Y.; Tang, G.; Sun, X.; Yang, F.; Shi, H.; Liu, Z.; Qin, L. An all-inorganic Li-doped $Cs_3Cu_2I_5$ single crystal for dual gamma ray and neutron detection applications. *J. Mater. Chem. C* **2022**, *10*, 15400-15407.

[12] Xie, L.; Chen, B.; Zhang, F.; Zhao, Z.; Jiang, T.; Wang, M.; Wu, Y.; Huang, L.; Song, W.; Liu, Y.; Wang, Y. Stability enhancement of $Cs_3Cu_2I_5$ powder with high blue emission realized by Na^+ doping strategy. *J. Lumin.* **2021**, *239*, 118333.

[13] Guo, N.; Liu, L.; Cao, G.; Xing, S.; Liang, J.; Chen, J.; Tan, Z.; Shang, Y.; Lei, H. Enhancing emission and stability in Na-doped $Cs_3Cu_2I_5$ nanocrystals. *Nanomaterials* **2024**, *14*, 1118.

[14] Tang, Y.; Xie, Q.; Zhang, X.; Ma, J.; Xie, H.; Liu, Y.; Zhao, L.; Yan, D.; Wang, X.; Ye, W. Scalable open-air synthesis of Mg^{2+}-doped lead-free $Cs_3Cu_2Cl_5$ nanocrystals for high-performance green LEDs. *Laser Photonics Rev.* **2025**, *19*, 2500430.

[15] Wu, Y.; Lu, M.; Lu, P.; Liu, M.; Li, R.; Liu, Y.; Feng, J.; Zhang, F.; Wu, Z.; Zhang, Y.; Bai, X.; Tang, A. Mg^{2+}-doped cesium copper halide for bright electroluminescent white light-emitting diodes. *Adv. Funct. Mater.* **2024**, *35*, 2414456.

[16] Wang, Y.; Chen, X.; Qin, W.; Wang, Z.; Zhao, D.; Liu, Y.; Jia, M.; Li, X.; Shi, Z. Enhanced photoluminescence of dual Mn(II)-Based all-inorganic perovskite nanocrystals via Ce^{3+} doping for white light-emitting diodes and anti-counterfeiting. *J. Lumin.* **2026**, *293*, 121861

[17] Chen, J.; Li, J.; Yin, T.; Yin, Z.; Li, Y.; Wang, C.; Guan, L.; Xiao, J.; Teng, F.; Tang, A. Rb-Doped $Cs_3Cu_2I_5$ Perovskite Nanocrystals as Paper-Based Scintillator Film for High-Resolution X-Ray Imaging. *Adv. Funct. Mater.* **2025**, *35*, 2506331

[18] Cui, W.; Zhao, J.; Wang, L.; Lv, P.; Li, X.; Yin, Z.; Yang, C.; Tang, A. Unraveling the phase transition and luminescence tuning of Pb-free Cs-Cu-I perovskites enabled by reaction temperature and polar solvent. *J. Phys. Chem. Lett.* **2022**, *13*, 4856-4863.

[19] Chen, Z.; Dhakal, T. P. Room temperature synthesis of lead-free $FASnI_3$ perovskite nanocrystals with improved stability by SnF_2 additive. *Appl. Phys. Rev.* **2023**, *10*, 011404.

[20] Chowdhury, T. H.; Reo, Y.; Yusoff, A. R. B. M.; Noh, Y. Y. Sn-based perovskite halides for electronic devices. *Adv. Sci.* **2022**, *9*, 2203749.

[21] Wang, A.; Yan, X.; Zhang, M.; Sun, S.; Yang, M.; Shen, W.; Pan, X.; Wang, P.; Deng, Z. Controlled synthesis of lead-free and stable perovskite derivative Cs_2SnI_6 nanocrystals via a facile hot-injection process. *Chem. Mater.* **2016**, *28*, 8132-8140.

[22] Kang, L.; Lin, Z. Regulation strategy of white emission from organic-inorganic hybrid metal halide perovskites. *Inorg. Chem.* Frontiers **2023**, *10*, 13-36.

[23] Wang, Z.; Wei, Y.; Liu, C.; Liu, Y.; Hong, M. Mn^{2+}-activated $Cs_3Cu_2I_5$ nano-scintillators for ultra-high resolution flexible X-ray imaging. *Laser Photonics Rev.* **2023**, *17*, 2200851.

[24] Yan, X.; Hu, Y.; Wan, N.; Pang, Q.; Chen, Y. Mild and rapid solution synthesis of Mn^{2+}-doped $Cs_3Cu_2I_5$ microcrystals. *Chin. J. Lumin.* **2024**, *45*, 375-382.

[25] Yan, X.; Zhou, Y.; Wang, Q.; Zhang, J. Z.; Chen, Y.; Pang, Q.; Liu, Z. Q. Enhancing initial surface adsorption for doped lead-free copper(I) halide microcrystals through a moderate Lewis base ligand. *Adv. Funct. Mater.* **2024**, *34*, 2311106.

[26] Zhang, J.; Han, Y.; Zhang, L.; Zhu, H.; Song, T.; Yan, D.; Zhang, M.; Wang, C.; Zhang, X. Dual color luminescence of Mn^{2+} doped lead-free $Cs_3Cu_2I_5$ perovskite phosphors and their LED solid-state lighting and anti-counterfeiting applications. *Mater. Res. Bull.* **2023**, *164*, 112241.

[27] Chen, J.; Shang, B.; Li, Y.; Yin, Z.; Teng, F.; Tang, A. Energy-level-

dominated luminescence tuning of Mn^{2+}-doped $Cs_3Cu_2I_5$ perovskites for single-component white LEDs. *Opt. Lett.* **2025**, *50*, 6081.

[28] Li, C. X.; Cho, S. B.; Sohn, S. H.; Kwak, D. H.; Park, I. K. Full-color gamut white light emission from Mn-doped $Cs_3Cu_2X_5$ nanocrystals via lattice engineering. *Small* **2025**, *21*, 2408468.

[29] Wang, Z.; Deng, X.; Chen, X.; Qin, W.; Wang, M.; Zai, Y.; Jia, M.; Liu, Y.; Ma, Z.; Zhang, J.; Lian, L.; Han, Y.; Tian, Y.; Wu, D.; Li, X.; Xu, W.; Shi, Z. Efficient ultraviolet emission via Ce^{3+}-doped lead-free double perovskite nanocrystals for multicolor and full-spectrum luminescence. *Chem. Eng. J.* **2026**, *535*, 175550.

[30] Wu, Y.; Li, X.; Zeng, H. Lead-free halide double perovskites: structure, luminescence, and applications. *Small Struct.* **2020**, *2*, 2000071.

[31] Hui, Y.; Chen, S.; Lin, R.; Zheng, W.; Huang, F. Photophysics in $Cs_3Cu_2I_5$ and $CsCu_2I_3$. *Mater. Chem. Front.* **2021**, *5*, 7088-7107.

[32] Xing, Z.; Zhou, Z.; Zhong, G.; Chan, C. C. S.; Li, Y.; Zou, X.; Halpert, J. E.; Su, H.; Wong, K. S. Barrierless exciton self-trapping and emission mechanism in low-dimensional copper halides. *Adv. Funct. Mater.* **2022**, *32*, 2207638.

[33] Liu, S.; Yue, Y.; Zhang, X.; Wang, C.; Yang, G.; Zhu, D. A controllable and reversible phase transformation between all-inorganic perovskites for white light emitting diodes. *J. Mater. Chem. C* **2020**, *8*, 8374-8379.

[34] Lian, L.; Zheng, M.; Zhang, P.; Zheng, Z.; Du, K.; Lei, W.; Gao, J.; Niu, G.; Zhang, D.; Zhai, T.; Jin, S.; Tang, J.; Zhang, X.; Zhang, J. Photophysics in $Cs_3Cu_2X_5$ (X = Cl, Br, or I): Highly luminescent self-trapped excitons from local structure symmetrization. *Chem. Mater.* **2020**, *32*, 3462-3468.

[35] Li, X.; Li, W.; Xia, M.; Liu, C.; Li, N.; Shi, Z.; Xu, Y.; Zhang, X. Facile melting-crystallization synthesis of $Cs_2Na_xAg_{1-x}InCl_6$: Bi double perovskites for white light-emitting diodes. *Inorg. Chem.* **2022**, *61*, 5040-5047.

[36] Chen, Y.; Zhu, H.; Babaian, D.; Dzorkpata, C.; Grigoriev, A.; Wang, Z.; Wheat, S.; Guha, S.; Zhu, P. Near-unity PLQY of $Cs_3Cu_2X_5$ (X = Cl, Br) for high‐efficiency white light‐emitting diodes with exceptional color quality. *Adv. Mater.* **2025**, *37*, 2500083.

Electronic Supplementary Material

Zn^{2+}-doped Cs-Cu-I perovskite nanocrystals for white light-emitting diodes with high color rendering index

Jie Chen [1], Zhe Yin [1] ✉, Tao Yin [2], Jinxing Zhao [2], Yu Li [1], Li Guan [2], Feng Teng [1] ✉, and Aiwei Tang [1] ✉

[1] *Key Laboratory of Luminescence and Optical Information, Ministry of Education, School of Physical Sciences and Engineering, Beijing Jiaotong University, Beijing 100044, China*
[2] *Hebei Key Laboratory of Photo-Electricity Information and Materials, College of Physics Science and Technology, Hebei University, Baoding 071002, China*

Received: 30 May 2026; **Revised:** 4 July 2026; **Accepted:** 12 July 2026

✉ Address correspondence to Aiwei Tang, awtang@bjtu.edu.cn; Feng Teng, fteng@bjtu.edu.cn; Zhe Yin, zheyin@bjtu.edu.cn

Supporting information to https://doi.org/10.26599/NR.2026.94909020

DFT calculation

All calculations are calculated by density functional theory (DFT) based on Vienna Ab Initio Simulation Package (VASP) [1]. The generalized gradient approximation (GGA) of the Perdewe-Burkee-Ernzerhof (PBE) is used to approximate the exchange correlation potential [2, 3]. The cut-off energy for the plane wave basis was set to be 500 eV, and a 2 × 2 × 2 Monkhorst-Pack grid was employed. The convergence criteria for the energy and forces were set as 10-5 eV and 0.05eV/Å, respectively.

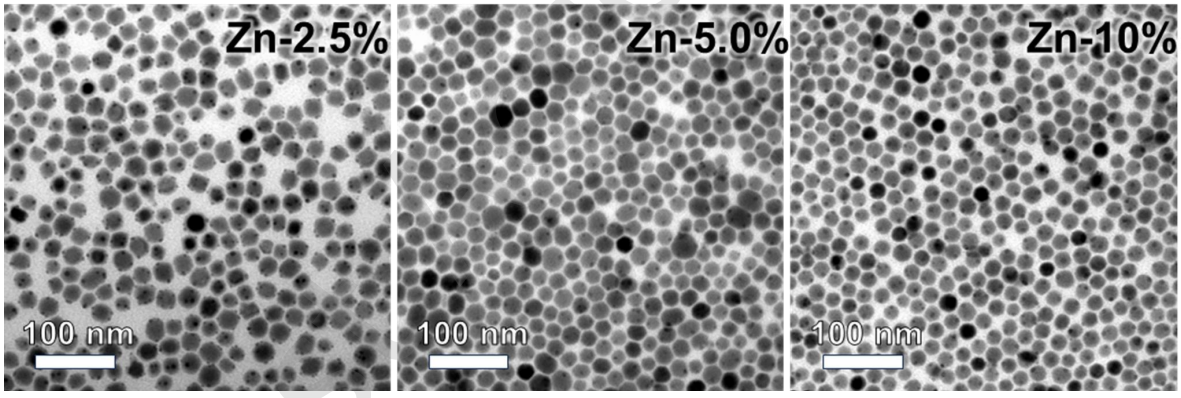

Figure S1. TEM images of $Cs_3Cu_2I_5$: x% Zn NCs (x = 2.5%, 7.5%, and 10%).

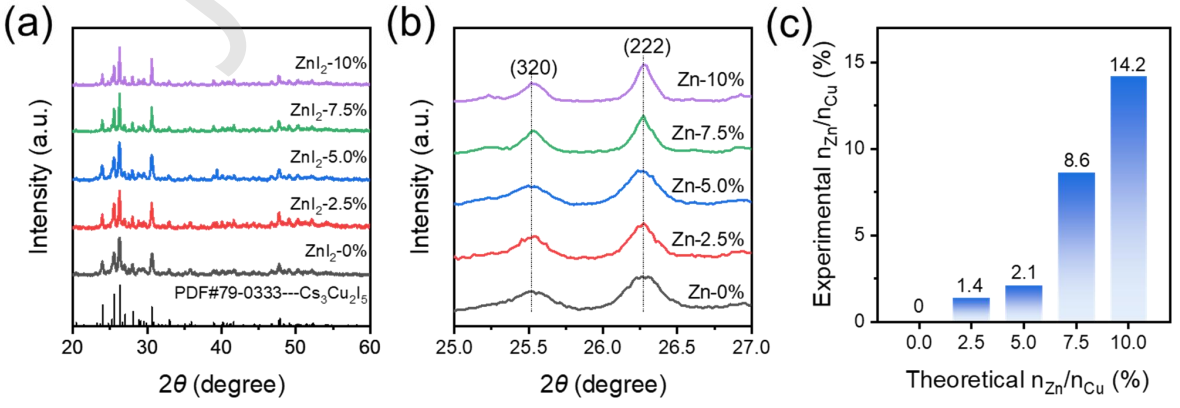

Figure S2. (a) XRD patterns and (b) their partially enlarged images of $Cs_3Cu_2I_5$ NCs with different Zn^{2+} doping amounts; (c) actual Zn^{2+} content in $Cs_3Cu_2I_5$: Zn NCs measured by ICP.

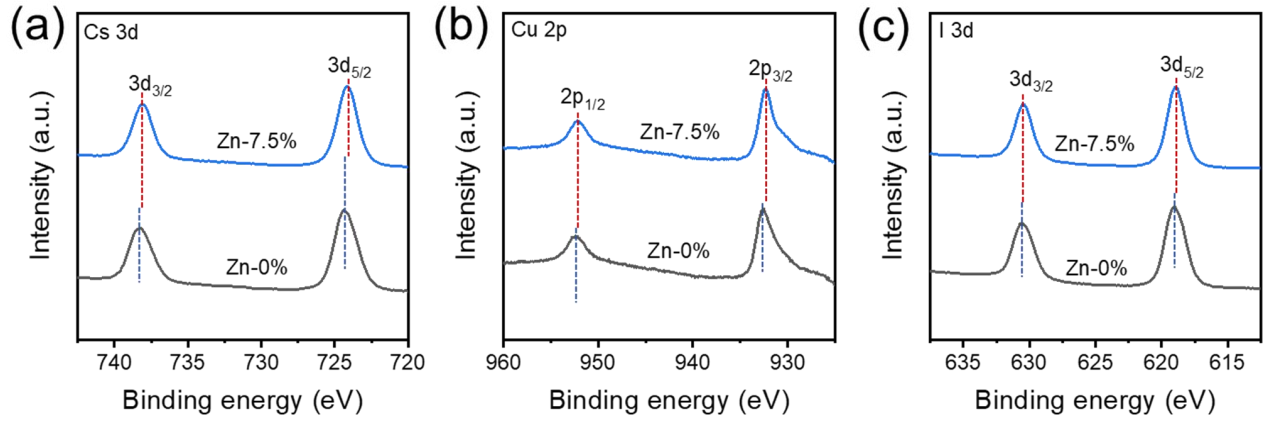

Figure S3. XPS spectra of undoped $Cs_3Cu_2I_5$, and $Cs_3Cu_2I_5$: 7.5%Zn: (a) Cs 3d, (b) Cu 2p, and (c) I 3d.

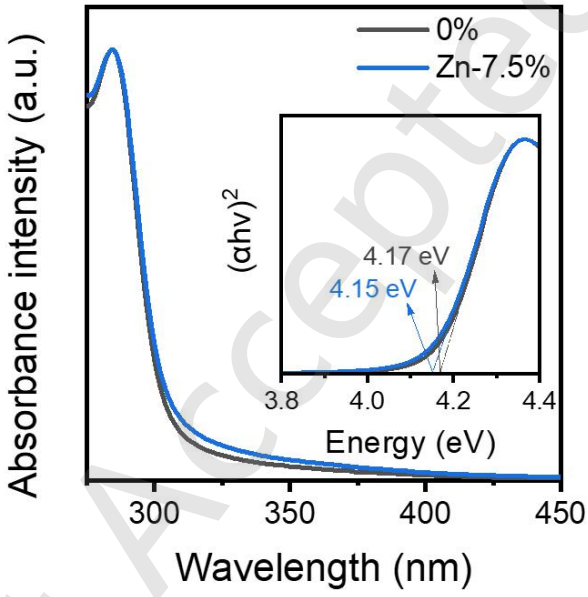

Figure S4. Absorption spectra (inset: corresponding Tauc plots) of undoped $Cs_3Cu_2I_5$, and $Cs_3Cu_2I_5$: 7.5%Zn.

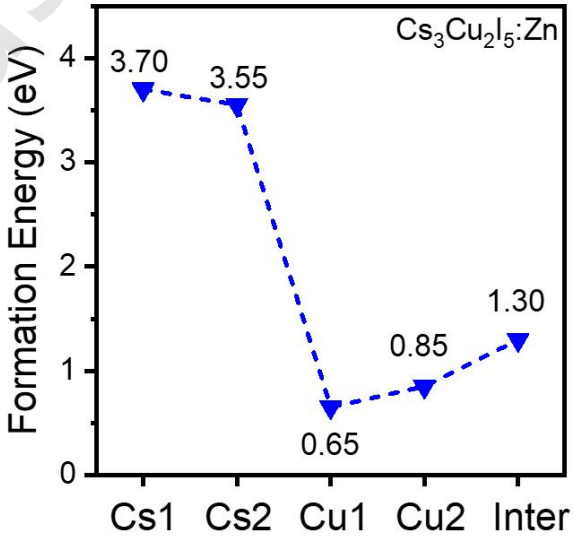

Figure S5. The doping formation energy of Zn at different sites.

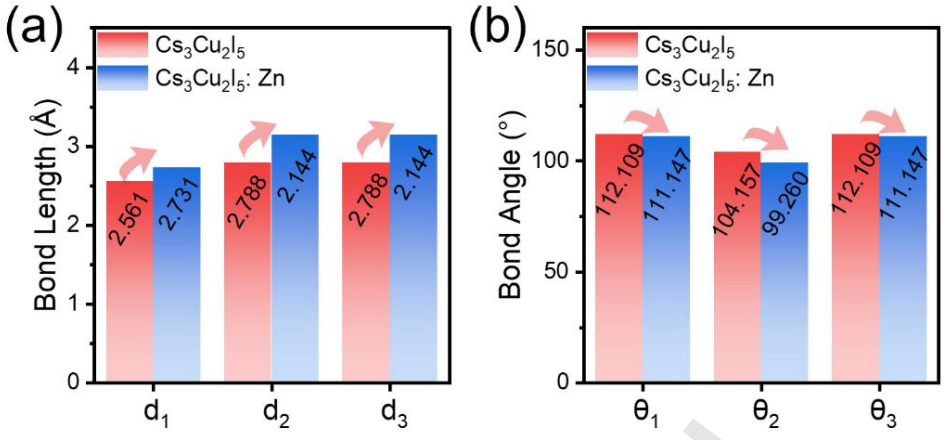

Figure S6. (a) The bond lengths and (b) the bond angles between B and I atoms in $Cs_3Cu_2I_5$ before and after doping with Zn^{2+}.

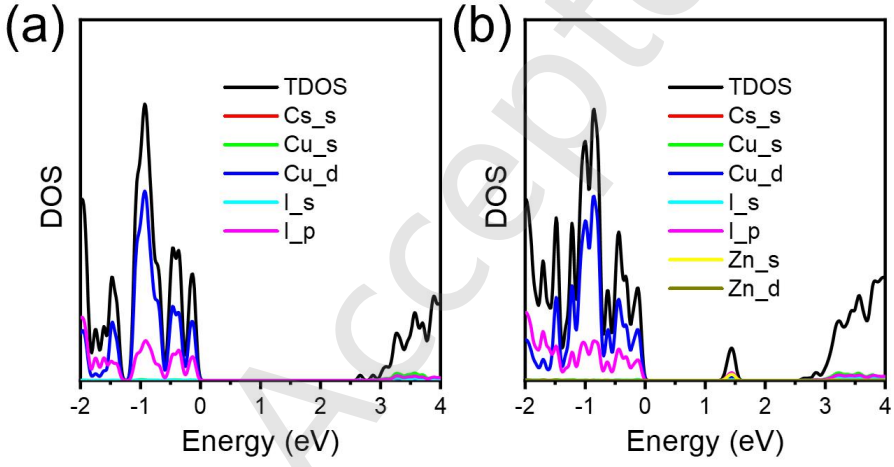

Figure S7. DFT calculations: The density of states of (a) $Cs_3Cu_2I_5$, and (b) $Cs_3Cu_2I_5$: Zn.

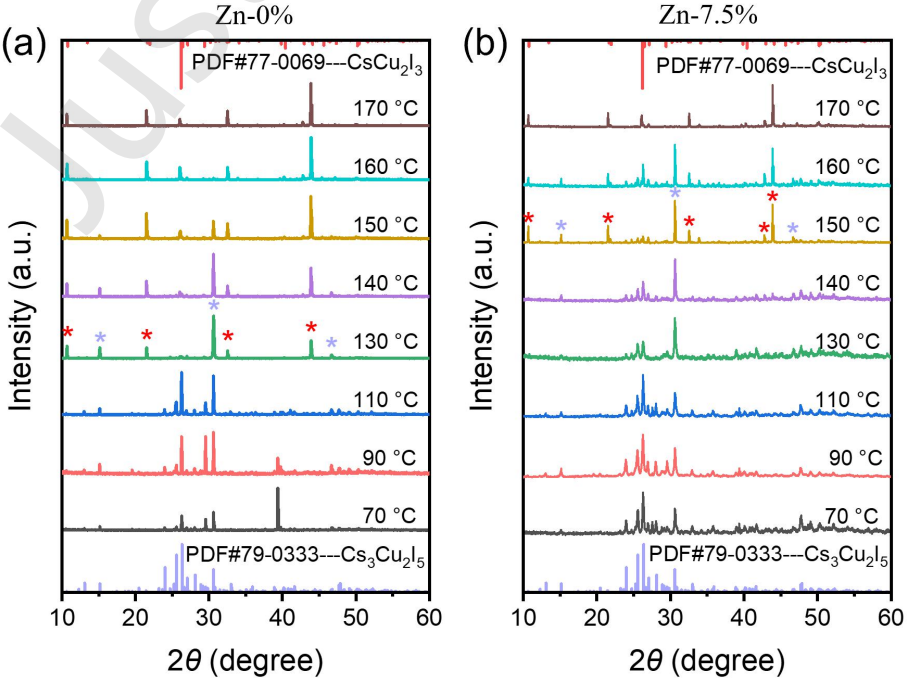

Figure S8. XRD patterns of (a) Cs-Cu-I and (b) Cs-Cu-I: 7.5%Zn synthesized at different reaction temperatures.

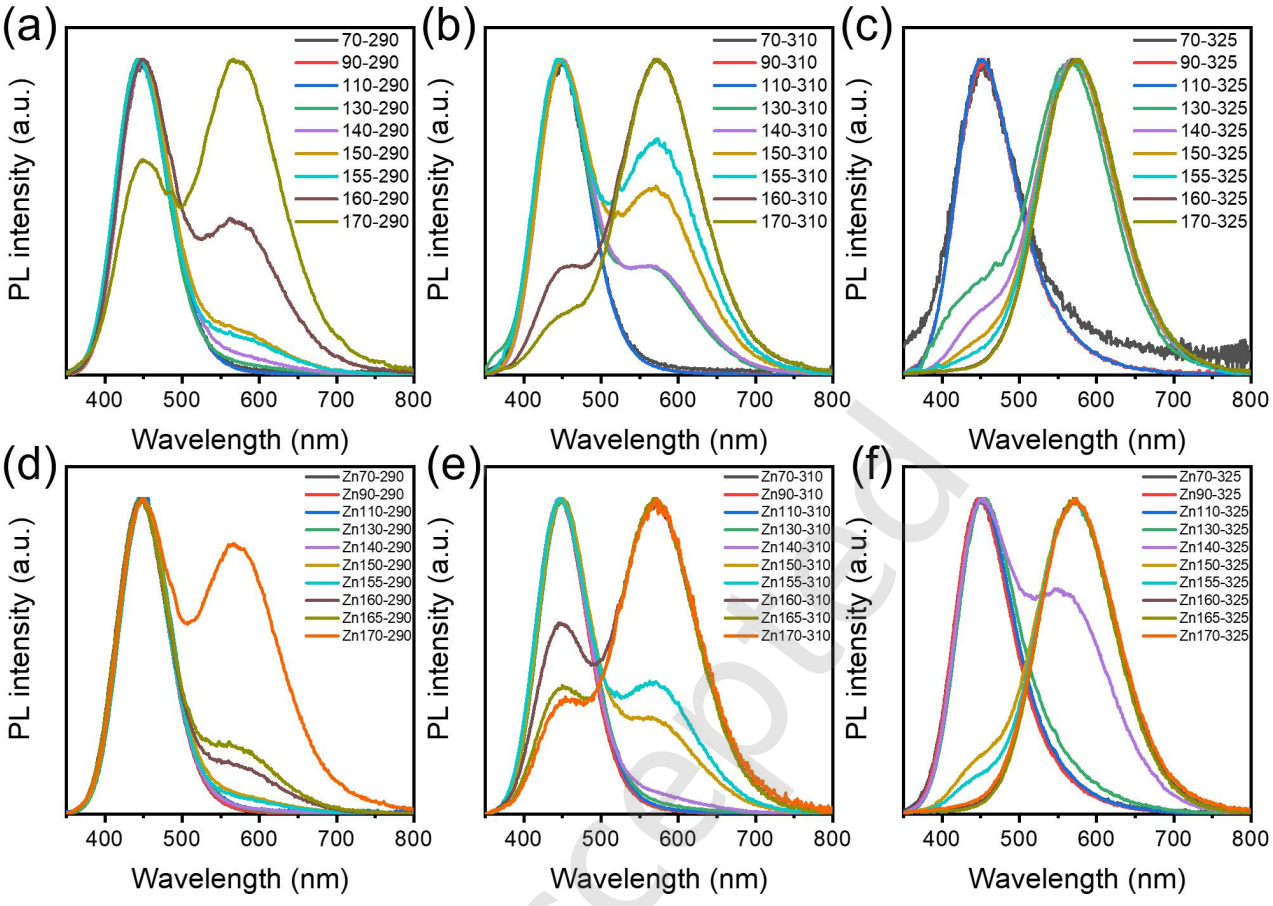

Figure S9. PL spectra of (a-c) Cs-Cu-I and (d-f) Cs-Cu-I: 7.5%Zn synthesized at different reaction temperatures under 290 nm, 310 nm and 325 nm ultraviolet light excitation.

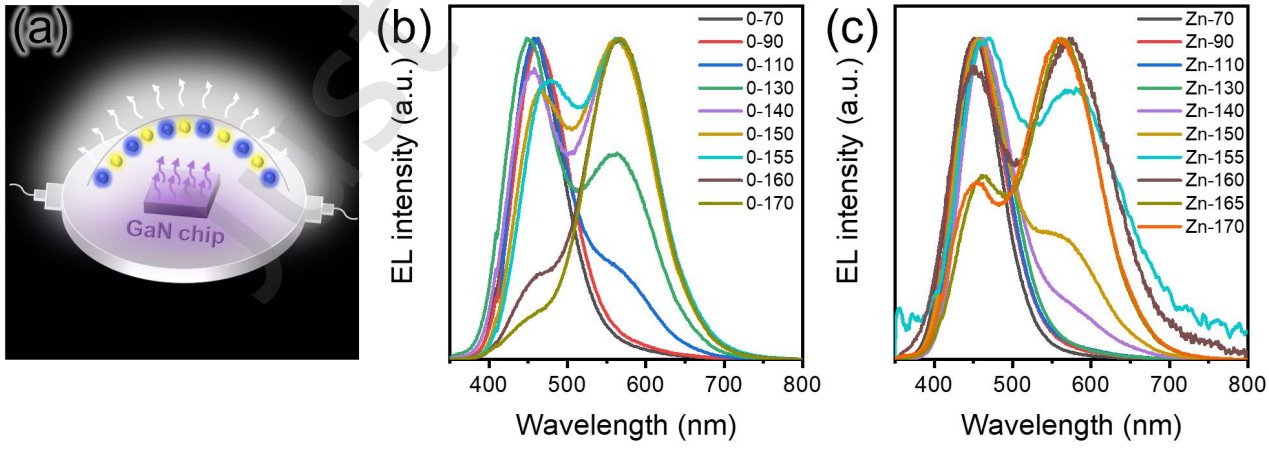

Figure S10. (a) Device structure diagram of the WLEDs; EL spectra of WLEDs devices fabricated with (b) Cs-Cu-I and (c) Cs-Cu-I: 7.5%Zn synthesized at different reaction temperatures.

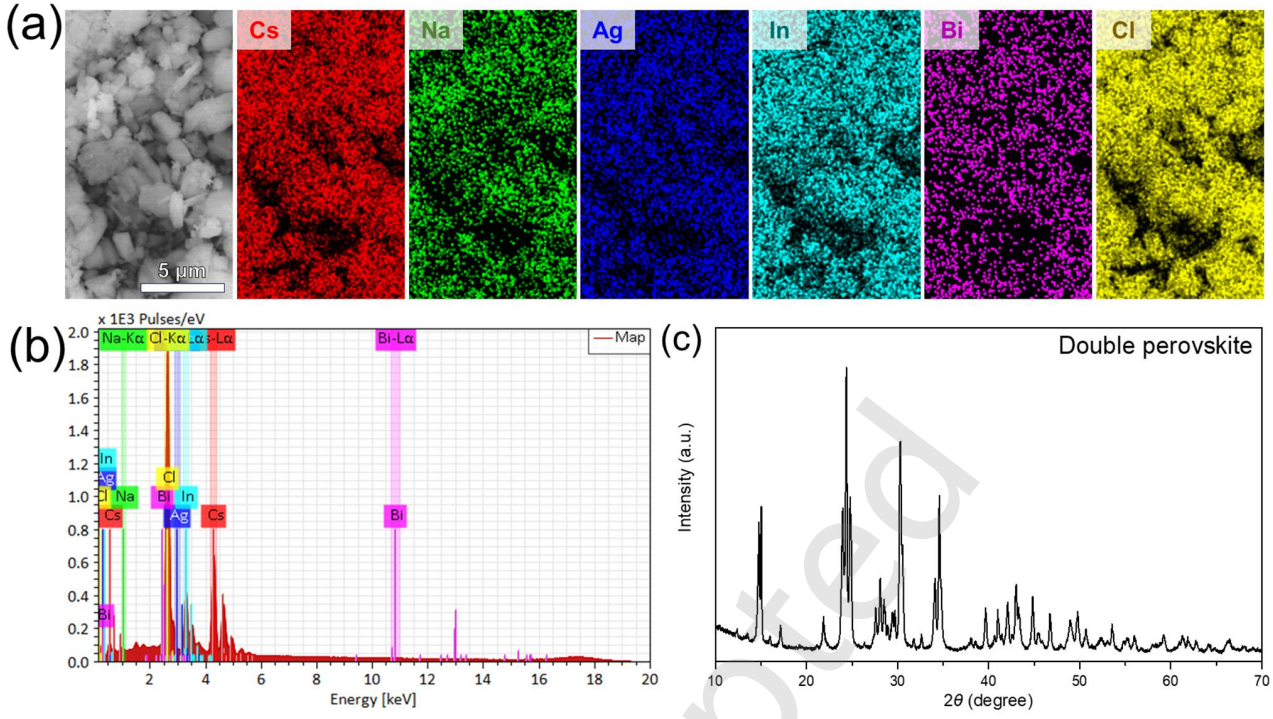

Figure S11. (a) FESEM image and the corresponding EDS element mapping, (b) EDX spectrum, and (c) XRD pattern of double perovskite.

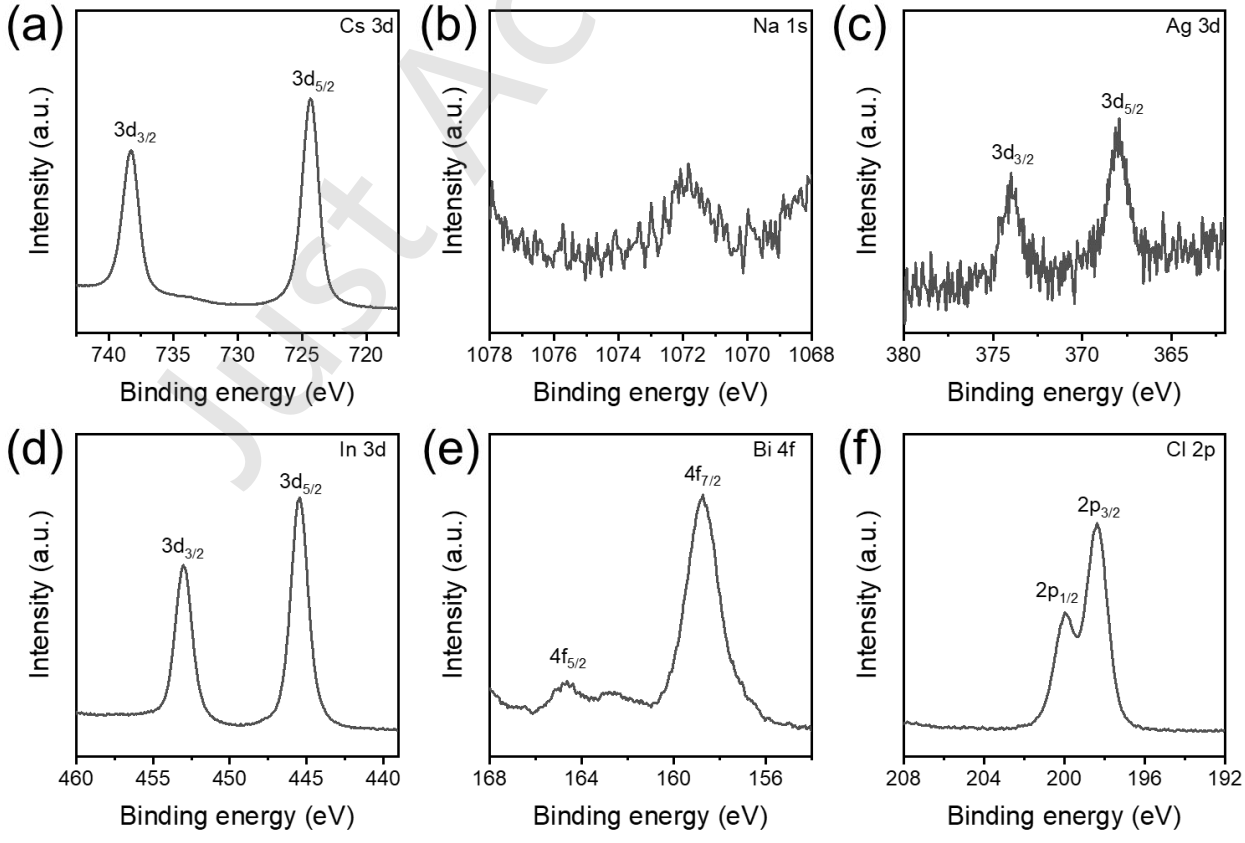

Figure S12. XPS spectra of the double perovskite: (a) Cs 3d, (b) Na 1s, (c) Ag 3d, (d) In 3d, (e) Bi 4f, and (f) Cl 2p.

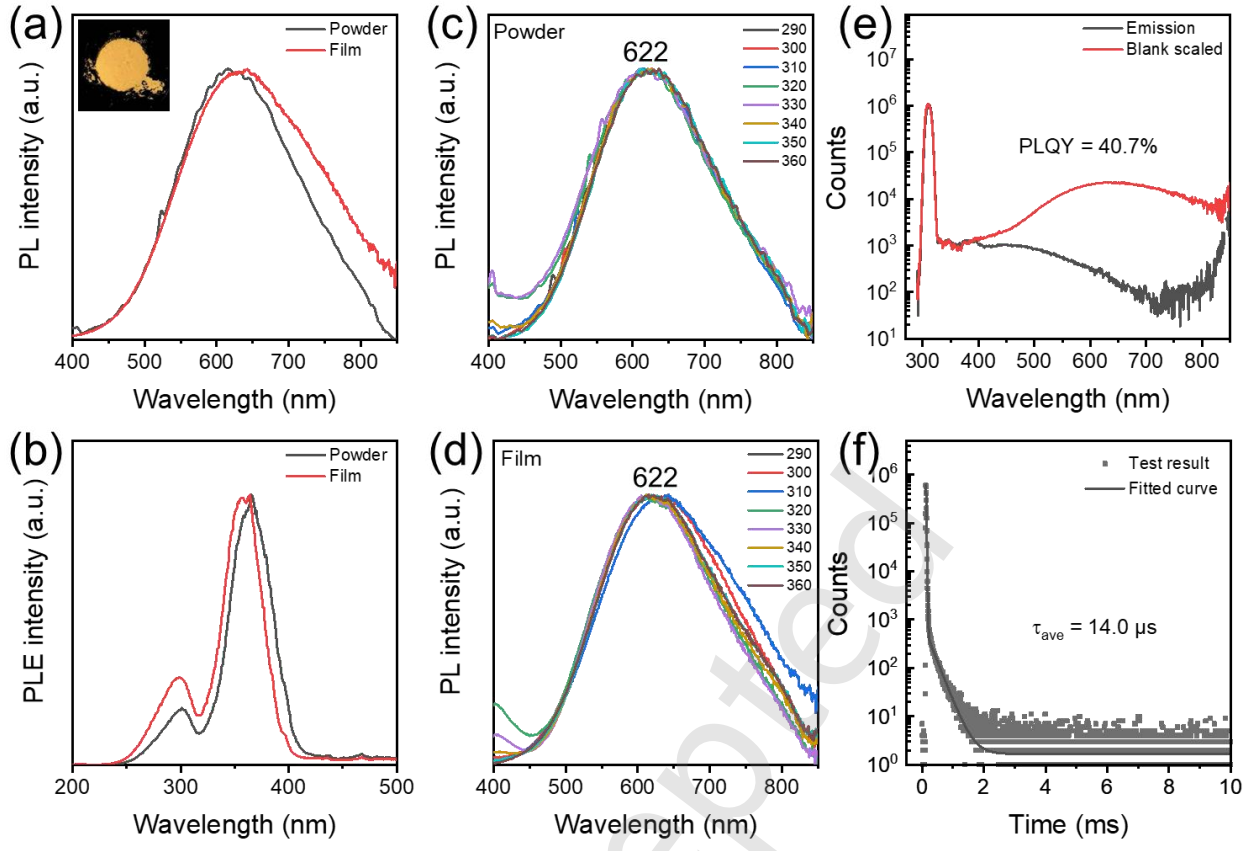

Figure S13. Optical characterization of double perovskite powder and film: (a) PL spectra under 310 nm excitation and (b) corresponding PLE spectra monitored at the 622 nm emission peak; (c) PL spectra of powder and (d) film under different ultraviolet excitation wavelengths; (e) absolute PLQY of the powder and (f) TRPL decay curves.

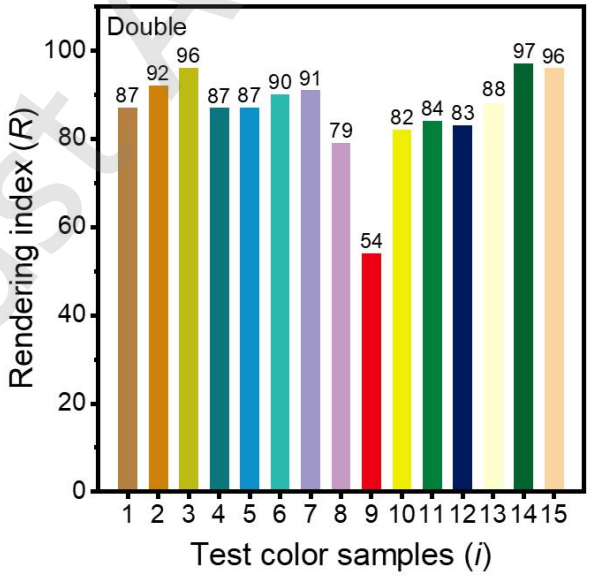

Figure S14. R_1-R_{15} special color rendering index of the LED device fabricated with double perovskite.

Double perovskite	a (Å)	9.8615, 0.14)	11.0	14.39	(0.15, 0.10)	266	14.23	14.0
90 °C	b (Å)	(0.16, 0.17)		10.15	-	47.13	(0.15, 0.12)	24.29
110 °C	c (Å)	(0.21, 0.23)		11.68	-	0.03	(0.15, 0.13)	0.10
130 °C	α (°)	(0.27, 0.29)		90	80	0.08	(0.15, 0.15)	90
140 °C	β (°)	(0.32, 0.35)		90	74	18.96	(0.19, 0.20)	11.31
150 °C	γ (°)	(0.32, 0.38)		90	70	0.66	(0.23, 0.24)	92.26
155 °C	Unit-cell volume (Å^3)	(0.33, 0.38)		1704.27	71	33.14	(0.31, 0.33)	1672.46
160 °C	Space group name	(0.39, 0.46)		Pbnm	-		(0.33, 0.34)	P1
165 °C		-		-			(0.34, 0.40)	
170 °C		(0.41, 0.49)		-			(0.34, 0.40)	

Element Mass percent (%) Atomic percent (%)
Cs 47.13 24.29
Na 0.03 0.10
Ag 0.08 0.05
Zn 18.96 11.31
Br 0.66 0.22
Cl 33.14 64.03

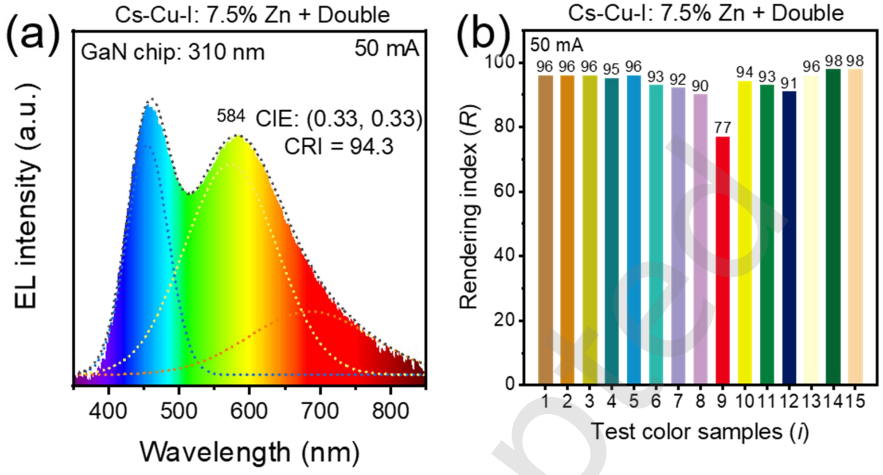

Figure S15. Characterization of the WLED device fabricated based on Cs-Cu-I: 7.5%Zn and double perovskite under 50 mA operating currents: (a, b) EL spectra and (c, d) R_1-R_{15} special color rendering index.

Table S1. Lattice parameters of $Cs_3Cu_2I_5$ and $Cs_3Cu_2I_5$: Zn.

lattice parameter	$Cs_3Cu_2I_5$	$Cs_3Cu_2I_5$: Zn

Table S2. CIE and CRI of WLEDs devices fabricated with Cs-Cu-I and Cs-Cu-I: 7.5% Zn synthesized at different reaction temperatures.

Sample	Cs-Cu-I		Cs-Cu-I: 7.5% Zn	
	CIE	CRI	CIE	CRI

Table S3. Elemental composition of the double perovskite determined by EDX spectrum analysis.

Table S4. Fitting results of TRPL spectra of double perovskite.

Sample	α_1 (%)	τ_1 (μs)	α_2 (%)	τ_2 (μs)	τ_{ave} (μs)

Table S5. Luminous performance parameters of the fabricated WLEDs.

Sample parameters	Cs-Cu-I: 7.5% Zn	Double perovskite	Cs-Cu-I: 7.5% Zn + Double perovskite							
			20 mA	30 mA	40 mA	50 mA	60 mA	70 mA	80 mA	90 mA	100 mA

CRI	89.2	88.7	92.7	93.4	93.8	94.3	94.2	94.5	94.4	94.5	94.5
R_i	89.2	86.9	91.2	91.7	92.2	92.7	92.9	93.9	93.5	94.0	94.0
R_g	93.6	99.7	98.9	99.3	99.6	100	99.9	100.6	100.4	100.7	100.6
R_1	89	87	94	95	95	96	96	96	96	95	96
R_2	98	92	97	97	97	96	96	95	95	95	95
R_3	92	96	95	95	95	96	95	96	95	95	95
R_4	85	87	92	93	94	95	95	96	96	96	96
R_5	90	87	95	96	96	96	96	96	96	95	95
R_6	96	90	94	94	94	93	93	93	93	92	92
R_7	88	91	90	91	92	92	92	93	93	94	94
R_8	75	79	84	86	87	90	89	92	92	94	93
R_9	34	54	62	68	72	77	77	84	83	89	88
R_{10}	95	82	96	96	95	94	94	93	93	91	91
R_{11}	85	84	90	91	92	93	93	94	94	94	94
R_{12}	89	83	93	92	92	91	91	90	90	90	90
R_{13}	92	88	95	96	96	96	96	95	96	95	95
R_{14}	96	97	98	98	98	98	98	98	98	98	98
R_{15}	84	96	93	95	96	98	98	99	99	98	98
AveR	85.8	85.6	91.2	92.9	92.8	93.5	93.4	94.0	93.9	94.0	94.0
x	0.31	0.45	0.34	0.34	0.34	0.33	0.33	0.33	0.33	0.32	0.32
y	0.33	0.40	0.34	0.33	0.33	0.33	0.33	0.32	0.32	0.32	0.32
CCT (K)	6462	2791	5091	5281	5361	5588	5552	5861	5720	6065	5986

Table S6. Summary of luminous performance of WLEDs.

Material	CIE	CRI	Year	Ref
$CsPbBr_3$@APTES@BPSQ	(0.30, 0.31)	66.8	2024	[4]
$Cs_3Cu_2I_5$@$Gua_3Cu_2I_5$	(0.28, 0.34)	93	2024	[5]
$CsPbBr_3$@SiO_2@$MAlSiN_3$:Eu^{2+} (M = Ca, Sr)	(0.31, 0.37)	85	2025	[6]
$Cs_3Cu_2I_5$@$CsCu_2I_3$	(0.32, 0.33)	89.6	2025	[7]
$Cs_3Cu_2I_5$@$CsCu_2I_3$	(0.29, 0.32)	-	2025	[8]
$Cs_3Cu_2I_5$: $MnCl_2$	(0.34, 0.32)	-	2025	[9]
$Cs_3Cu_2I_5$: 7.5 Zn	(0.31, 0.33)	89	This work	
$Cs_3Cu_2I_5$: 7.5 Zn + double perovskite	(0.33, 0.33)	94.5		

References

[1] Kresse, G.; Furthmuller, J. Efficient iterative schemes for ab initio total-energy calculations using a plane-wave basis set. *Phys. Rev. B* **1996**, *54*, 11169-11186.

[2] Perdew, J. P.;Burke, K.; Ernzerhof, M. Generalized gradient approximation made simple (vol 77, pg 3865, 1996). *Phys. Rev. Lett.* **1997**, *78*, 1396-1396.

[3] Blochl, P. E. Projector augmented-wave method. *Phys. Rev. B:Condens. Matter* **1994**, *50*, 17953-17979.

[4] Ma, C.; Zhang, M.; Zhang, J.; Liao, J.; Sun, H.; Ji, D.; Pang, R.; Zhang, H.; Liu, J.; Liu, S. Highly luminescent and stable perovskite quantum dots films for light-emitting devices and information encryption. *Adv. Funct. Mater.* **2024**, *34*, 2316717.

[5] Zhang, W.; Chu, Z.; Jiang, J.; Zhang, S.; Hao, H.; Wei, T.; Zhang, X.; You, J. High-performance white emission from Cu-based perovskite compound. *Adv. Opt. Mater.* **2024**, *12*, 2400092.

[6] Wu, X.; Wang, L.; Zhang, G.; Ma, L.; Wang, D.; Zhang, Y.; Bao, Y.; Wu, X.; Li, X.; Hu, Y.; Peng, H.-s. Highly stable and monodispersed silica-coated $CsPbBr_3$ perovskite quantum dots as ultraefficient light conversion phosphors for micro-light-emitting diodes. *ACS Nano* **2025**, *19*, 29470-29480.

[7] Zhu, Y.; Kang, Y.; Su, J.; Wen, Z.; Li, M.; Zhu, Q.; Zhai, Y.; Kang, J.; Li, Y.; Wang, L. Mechanochemical synthesis of phase-pure $CsCu_2I_3$ and $Cs_3Cu_2I_5$ phosphors regulated by polar solvents and their application in tunable chromaticity LEDs. *Inorg. Chem.* **2025**, *64*, 1569-1578.

[8] Li, C. X.; Cho, S. B.; Park, I. K. Role of pseudohalide for enhancements of emission efficiency and stability of lead-free blue-emitting $Cs_3Cu_2I_5$ nanocrystals. *Adv. Opt. Mater.* 2025, 13, 2500072.

[9] Li, C. X.; Cho, S. B.; Sohn, S. H.; Kwak, D. H.; Park, I. K. Full-color gamut white light emission from Mn-doped $Cs_3Cu_2X_5$ nanocrystals via lattice engineering. *Small* **2025**, *21*, 2408468.